



# Understanding the Hydromechanical Behavior of a Fault Zone From Transient Surface Tilt and Fluid Pressure Observations at Hourly Time Scales

Jonathan Schuite, Laurent Longuevergne, Olivier Bour, Thomas J. Burbey,  
Fredrerick Boudin, Nicolas Lavenant, Philippe Davy

## ► To cite this version:

Jonathan Schuite, Laurent Longuevergne, Olivier Bour, Thomas J. Burbey, Fredrerick Boudin, et al.. Understanding the Hydromechanical Behavior of a Fault Zone From Transient Surface Tilt and Fluid Pressure Observations at Hourly Time Scales. *Water Resources Research*, 2017, 53 (12), pp.10558-10582. 10.1002/2017WR020588 . insu-01674282

HAL Id: insu-01674282

<https://insu.hal.science/insu-01674282>

Submitted on 2 Jan 2018

**HAL** is a multi-disciplinary open access archive for the deposit and dissemination of scientific research documents, whether they are published or not. The documents may come from teaching and research institutions in France or abroad, or from public or private research centers.

L'archive ouverte pluridisciplinaire **HAL**, est destinée au dépôt et à la diffusion de documents scientifiques de niveau recherche, publiés ou non, émanant des établissements d'enseignement et de recherche français ou étrangers, des laboratoires publics ou privés.



## Water Resources Research

### RESEARCH ARTICLE

10.1002/2017WR020588

#### Key Points:

- Tilt time series from long baseline tiltmeters clearly record transient mechanical signature of pressure variations due to pumping in a fault
- Tilt measurements on both sides of an hydraulically active fault zone help constraining its diffusivity and elastic properties
- Hydraulic diffusivity contrast and flow dynamics between fault and matrix can be apprehended from tilt over pore pressure change ratios

#### Supporting Information:

- Supporting Information S1

#### Correspondence to:

J. Schuite,  
jonathan.schuite@univ-rennes1.fr;  
L. Longuevergne,  
laurent.longuevergne@univ-rennes1.fr

#### Citation:

Schuite, J., Longuevergne, L., Bour, O., Burbey, T. J., Boudin, F., Lavenant, N., & Davy, P. (2017). Understanding the hydromechanical behavior of a fault zone from transient surface tilt and fluid pressure observations at hourly time scales. *Water Resources Research*, 53. <https://doi.org/10.1002/2017WR020588>

Received 14 FEB 2017

Accepted 7 NOV 2017

Accepted article online 10 NOV 2017

## Understanding the Hydromechanical Behavior of a Fault Zone From Transient Surface Tilt and Fluid Pressure Observations at Hourly Time Scales

Jonathan Schuite<sup>1</sup> , Laurent Longuevergne<sup>1</sup> , Olivier Bour<sup>1</sup>, Thomas J. Burbey<sup>2</sup>, Frédéric Boudin<sup>3</sup>, Nicolas Lavenant<sup>1</sup>, and Philippe Davy<sup>1</sup> 

<sup>1</sup>Géosciences Rennes, UMR-CNRS 6118, Université de Rennes 1, Rennes, France, <sup>2</sup>Department of Geosciences, Virginia Tech, Blacksburg, VA, USA, <sup>3</sup>Laboratoire de Géologie, UMR-CNRS 8538, Ecole Normale Supérieure, Paris, France

**Abstract** Flow through reservoirs such as fractured media is powered by head gradients which also generate measurable poroelastic deformation of the rock body. The combined analysis of surface deformation and subsurface pressure provides valuable insights of a reservoir's structure and hydromechanical properties, which are of interest for deep-seated CO<sub>2</sub> or nuclear waste storage for instance. Among all surveying tools, surface tiltmeters offer the possibility to grasp hydraulically induced deformations over a broad range of time scales with a remarkable precision. Here we investigate the information content of transient surface tilt generated by the pressurization a kilometer scale subvertical fault zone. Our approach involves the combination of field data and results of a fully coupled poromechanical model. The signature of pressure changes in the fault zone due to pumping cycles is clearly recognizable in field tilt data and we aim to explain the peculiar features that appear in (1) tilt time series alone from a set of four instruments and 2) the ratio of tilt over pressure. We evidence that the shape of tilt measurements on both sides of a fault zone is sensitive to its diffusivity and its elastic modulus. The ratio of tilt over pressure predominantly encompasses information about the system's dynamic behavior and extent of the fault zone and allows separating contributions of flow in the different compartments. Hence, tiltmeters are well suited to characterize hydromechanical processes associated with fault zone hydrogeology at short time scales, where spaceborne surveying methods fail to recognize any deformation signal.

### 1. Introduction

Naturally fractured reservoirs are relatively widespread on Earth and they are of common interest for a variety of societal and economical reasons. For example, these reservoirs may be exploited for the resources they bear or on the contrary, they can be considered for deep-seated storage reservoirs like carbon dioxide sequestration and nuclear waste disposal (Berkowitz, 2002). In the former case, the interest is often focused on the resource's sustainability and profitability whereas in the latter case, the emphasis is primarily on the risk assessment of potential reservoir failure, induced seismicity, and leakage. Therefore, characterizing the hydromechanical properties of fractured reservoirs is fundamental to achieve the sound and safe management of such geotechnical projects. Nevertheless, fractured geological media form complex systems due to their heterogeneous structure, anisotropy, and scale-dependent physical behavior (Berkowitz, 2002; Bonnet et al., 2001; Neuman, 2005). Their complexity arises especially from the fact that their properties may vary largely with both space and time, due to numerous interactions of processes, of which each may have its preponderance depending on the scale of interest.

From centimetric to metric scales, it is now broadly admitted that under certain conditions, fluid flow in fractured media can only be well understood and described using a fully coupled poromechanical modeling framework (Rutqvist & Stephansson, 2003). Indeed, a fracture undergoing a significant change in either pore pressure or effective stress will be deformed and this can be evidenced by laboratory experiments (Bandis et al., 1983; Barton et al., 1985; Elkoury et al., 2011), field tests (Cappa et al., 2006a, 2006b; Hisz et al., 2013; Karasaki et al., 2000; Schuite et al., 2017; Schweisinger et al., 2011; Svenson et al., 2008), or modeling (Murdoch & Germanovich, 2006; Schweisinger et al., 2009; Vinci et al., 2015; Wang & Cardenas, 2016). As their permeability is dependent on the cube of their hydraulic aperture, any opening or closing of a fracture

might have a noticeable impact on the flow field (Boussinesq, 1868; Witherspoon et al., 1980). Furthermore, when pore pressure or stress conditions vary largely enough, fractures may slip either abruptly or slowly, leading to seismogenic failures or aseismic slips respectively as discussed in the recent review by Cornet (2016). Accordingly, a natural seismic event can be responsible for an increase in a faulted reservoir's permeability (Elkoury et al., 2006; Kitagawa et al., 2002; Rojstaczer et al., 1995).

In fact, this important coupling between the physical properties of a fracture and its surrounding rock body on the one hand, and the flow on the other hand, has several practical consequences that can be applied in geotechnical engineering or may be used to gain knowledge about fractured reservoirs. For instance in reservoir stimulation, where the opening of existing fractures and the creation of new fractures are forced by strong hydraulic pulses to enhance the recovery of stored fluids, microseismic events are generally triggered (Davies et al., 2013; Warpinski et al., 2001) and may be used, for example, for fracture network characterization (Williams-Stroud et al., 2013) and hydraulic properties estimations (Rothert & Shapiro, 2003). In groundwater hydrology, hydromechanical well tests are shown to provide information on the geometry of fractures and of the preferential flow paths, and they are especially useful in complementing conventional hydraulic tests in order to better estimate the permeability and storativity of the medium (Murdoch & Germanovich, 2006, 2012; Rutqvist et al., 1998; Schuite et al., 2015; Schweisinger et al., 2009).

At larger spatial scales, from hundreds of meters to kilometers, conductive faults concentrate the main underground fluxes and therefore are responsible for much of the observable deformation. In this case, the surrounding fracture networks are often treated as equivalent homogeneous isotropic media, mostly because of the lack of information that precludes one from describing it with its detailed heterogeneities (Bense et al., 2013). For some faulted reservoirs, a fully coupled hydromechanical model is not necessary to interpret deformation data in the early development of a fluid pressure perturbation (pumping or recovery test) in order to provide information about the system (Schuite et al., 2015). In such case, the hypothesis of a pure elastic deformation of the fault is made during the early time when pressure diffusion is supposed to occur mainly within the most permeable part of the system, namely the fault itself. This simplifies the problem outstandingly and necessitates only modest computer resources to model and jointly interpret pressure and deformation data. It offers the potential of simply assessing the structural and hydraulic properties of a faulted reservoir. However at some point in the hydraulic experiment, the pressure diffuses significantly in the surrounding fracture networks and in the porous rock matrix which inevitably leads to poroelastic deformation of the system. Then, a simple elastic model seems to be largely unable to reproduce the deformation data (Schuite et al., 2015).

Many authors have studied faulted reservoirs from deformation observations. In order to achieve a sufficient spatial coverage of ground surface displacements, GPS or Interferometric Synthetic Aperture Radar (InSAR) is commonly used techniques (Biessy et al., 2011; Burbey, 2008; Chaussard et al., 2014; Galloway & Hoffmann, 2007; Vasco et al., 2010). They can measure net displacements in several directions, possibly down to millimeter accuracy, and therefore provide excellent constraints on the mechanical behavior and the structure of a faulted system that is being solicited by pumping or injection. Unfortunately, displacement measurements of a millimeter with these techniques demand low sampling rates, daily at best. This hampers the monitoring of hydraulic tests lasting only a few hours, or more generally, it may be difficult to capture the early signature of a transient hydraulic signal in the deformation data (for instance, see Moreau & Dauteuil, 2013). This is an important limitation since this particular time window links processes taking place at different temporal scales and possibly under different hydromechanical regimes.

Relative deformation instruments like tiltmeters or extensometers have emerged as interesting tools for groundwater hydrology (Barbour & Wyatt, 2014; Chen et al., 2010; Fabian & Kümpel, 2003; Longuevergne et al., 2009; Murdoch et al., 2015; Vasco et al., 2001). This is because they are able to record accurately and precisely small deformations at high sampling rates compared to spaceborne methods, up to 1 Hz. These instruments were originally designed for geophysical studies of the Earth's crust (seismology, volcanology, tectonics, etc.; Agnew, 1986) and have been increasingly utilized in the past decades as hydrogeophysical tools thanks to important technical developments that made them accurate enough to capture low amplitude hydrological signals (e.g., Boudin et al., 2008; Hisz et al., 2013). Despite the fact that they are sometimes not yet recognized among the hydrogeophysical community as recently suggested by Binley et al. (2015), relative deformation methods are noninvasive ways of monitoring transient subsurface flow.

In particular, tilt measurement is a method that is sensitive to a fault's geometry and hydromechanical parameters (Burbey et al., 2012; Hisz et al., 2013; Longuevergne et al., 2009; Schuite et al., 2015), even if it is not a proper measure of displacement but rather a measure of its gradient. Hence, the use of tiltmeters offers the unique possibility to grasp the full hydromechanical behavior of a fractured reservoir from the very beginning of a hydraulic perturbation and with a fine temporal resolution, high sensitivity, and good stability. Besides, it gives a complementary insight of pumping tests lasting only a few hours, which are the most common in hydrogeology. Indeed, hydraulic tests alone may reveal hydrodynamic properties of both fault zones and surrounding fractured media on the condition that many boreholes are covering the site and that many tests are performed, which can be impractical and costly. It is also worth pointing out that typical hydraulic tests in fractured media may fail to determine the transient evolution of flow geometry, and most often, numerous tests sampling different spatial scales are needed to evaluate all property contrasts. This is because these tests are either local (for example, cross-borehole flowmeter tests) or integrative (large scale pumping tests; Le Borgne et al., 2006). Hence, separating properties and responses of the different compartments of a faulted reservoir is not straightforward and surface deformation measurement may here add valuable constraints on these unresolved issues, as it is sensitive to both the mechanics and the flow dynamics of such a system.

Yet the full transient behavior of a tilt station, located at the surface near a fault where unsteady pressure conditions prevail, remains poorly understood. In particular, it is still unclear which information surface tilt data may reveal about the hydrodynamic behavior of each main compartment of a  $\sim 10^2$  to  $10^3$  m scale fractured reservoir. In the past decades, large efforts have been made to model and invert surface deformation data, but most of the time, the complexity of models and the duration of field tests precludes being able to reproduce and understand more than just the amplitudes of the measured signals. The work presented here aims at (1) demonstrating the usefulness of short hydromechanical experiments involving surface tilt monitoring to constrain key mechanical and flow properties of a faulted reservoir and (2) unraveling the information contained in complete transient tilt measurements about the dynamic behavior of this kind of system. In order to do so, we implement and analyze a fully coupled poromechanical model of a fault zone embedded in a porous matrix and confront numerical results with field data obtained at the Ploemeur hydrogeological observatory (Brittany, France).

## 2. The Ploemeur Hydrogeological Observatory and Field Data

### 2.1. The Experimental Site

The Ploemeur site (Figure 1) is located near the south coast of Brittany (France), a region shaped by several syntectonic intrusions of granitic rocks emplaced during the Hercynian orogeny. The Ploemeur fractured crystalline aquifer emerges from the intersection of two main structures (Ruelle et al., 2010): (1) a gently dipping contact zone between a granitic unit and an overlying mica-shist, striking East-West and (2) a dextral-slip normal fault zone striking N30°E and dipping steeply toward the West. The system is topped by a layer of clayed and sandy altered rock material with variable thickness generally ranging from 10 to 30 m. Three pumping boreholes drilled along the subvertical fault are exploited to supply about 20,000 inhabitants in the area, with withdrawal rates reaching  $130 \text{ m}^3/\text{h}$  (Schuite et al., 2015) and summing up to  $10^6 \text{ m}^3$  each year since 1991 (Le Borgne et al., 2004). This fairly good productivity given the geological context is thought to be intimately linked to the particular setting of the reservoir. In fact, the subhorizontal contact zone is capable of draining a vast area, from a far-end recharge zone to the fault, that allows for the vertical ascension of ground water fluxes toward the pumping site, which was the former natural outlet (humid zone) before the exploitation started (Jiménez-Martínez et al., 2013; Leray et al., 2012, 2013).

The site is monitored by several wells which are approximately 100 m deep and most often screened over their entire depth, except for the upper 20–40 m (Figure 1). We should point out that the aquifer exhibits a confined behavior based on geophysical evidence (Schuite et al., 2015) and the hydraulic signature of earth tides in piezometric observations.

As expected for fractured reservoirs, the Ploemeur aquifer is characterized by heterogeneous flow and hydrodynamic properties depending on fracture connectivity and scale of investigation. Indeed, the system displays an increase in transmissivity and storativity with the spatial and temporal scale of investigation, whereas the diffusivity decreases (Jiménez-Martínez et al., 2013; Le Borgne et al., 2004, 2006). Despite the

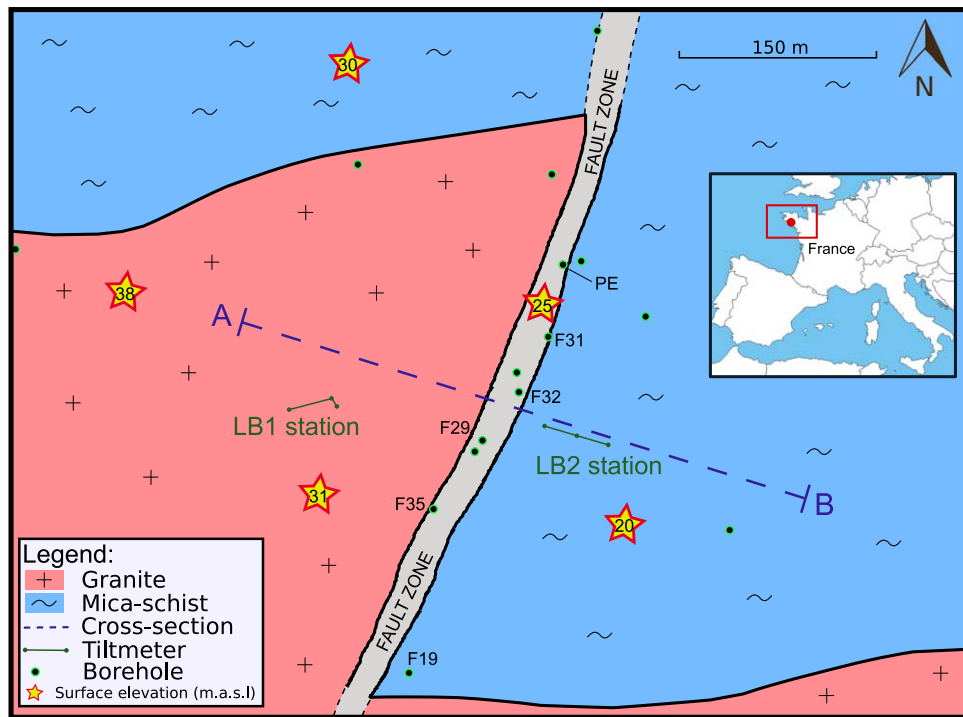


**Figure 1.** Localization and field setting of the Ploemeur site. The cross section AB is shown in Figure 2.

apparent complexity, its overall functioning can be synthesized in three main aspects when regarded at broad scale (i.e., at 100 m and more). (1) The contact zone controls the transfer of seasonal flow from an area north of the pumping site toward the pumped wells (Leray et al., 2013; Ruelleu et al., 2010).

(2) The fault zone, which is very diffusive, concentrates the flow at the vicinity of the pumped wells when the hydraulic perturbation lasts a few hours (Le Borgne et al., 2006). Moreover, this conductive structure almost exclusively controls the observed deformation at these short time scales (Schuite et al., 2015). (3) The granite and mica-schist units hold less permeable fracture networks, yet are well connected, embedded in their nearly impermeable crystalline matrix (Le Borgne et al., 2006). Hence, we consider at first order that this compartment forms an equivalent porous medium that is less transmissive than the previous two structures, but might still play a capacitive role in the system.

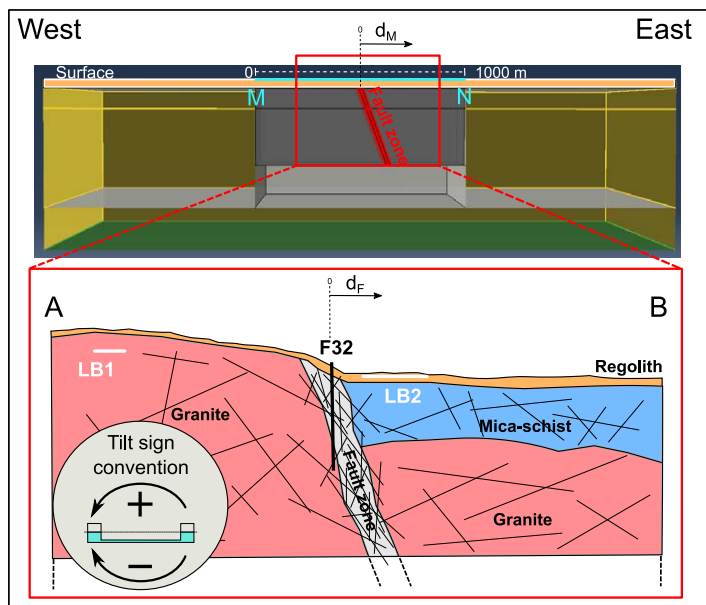


**Figure 2.** Structural analogy between the numerical model's geometry and the Ploemeur fractured aquifer. (top) Cross section of the 3-D model and position of MN profile delineated in Figure 6. (bottom) AB cross section of Ploemeur's aquifer as shown in Figure 1. The circular inset shows the sign convention used for observed and simulated tilt in this study. The red rectangles are meant to represent the link between modeled and natural hydrogeological structures, not scales.

## 2.2. Surface Deformation Monitoring

In addition to the hydrogeological studies and piezometric monitoring, the site is equipped with two tiltmeter stations which monitor surface deformation at a 30 s sampling rate. Each station is located at one side of the subvertical fault zone (Figures 1 and 2). These instruments measure the gradient of the surface's vertical displacement in one direction. The tiltmeters installed at these stations are called long baseline hydrostatic tiltmeters (LBHTs). Their measuring principle is rather simple as it works like a tube level (Figure 3). The devices consist of silica vessels linked by a pipe that are filled with water. The level of water in each vessel is precisely and continuously measured by a system comprising displacement transducers. Then, when a change in slope occurs, water flows from one vessel to the other to reach a new hydrostatic equilibrium. The difference in relative water level change

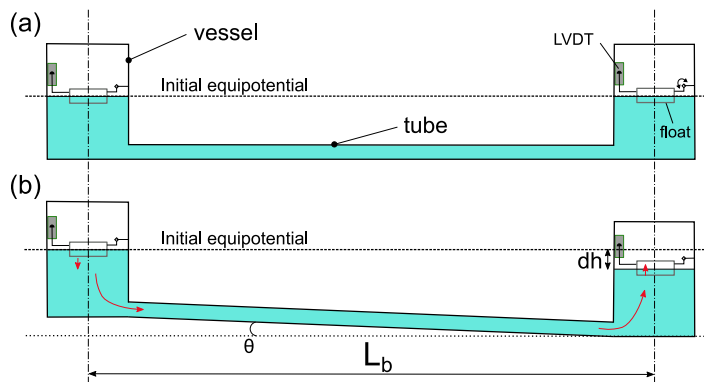


**Figure 3.** Measuring principle of the long baseline hydrostatic tiltmeters installed at the Ploemeur site. (a) Situation where the instrument is at equilibrium. (b) Situation immediately after a perturbation has occurred: a ground surface deformation causes, for instance, the right vessel to be relatively displaced downward. Consequently, a hydraulic gradient is formed between the two vessels, forcing the water to flow in order to reach a new equilibrium. This, of course, results in a relative change of water level in each vessel that is monitored by displacement transducers (LVDT). Tilt is then simply recovered as  $\theta = \tan(dh/L_b)$ , very well approximated by  $\theta = dh/L_b$  for small angles.

orientation of each LBHT and to estimate their distance to the N30°E-striking fault zone. The position of the fault's roof is approximately known from different geophysical and geological observations made in previous studies (Le Borgne et al., 2004, 2006; Ruelle et al., 2010; Schuite et al., 2015). Orientation and positioning data of all LBHT stations are summarized in Table 1. We have collected tilt data since May 2006 for LB1 station and since September 2011 for LB2 station.

### 2.3. Initial Findings From Hydromechanical Field Observations

Ground surface deformation due to pumping is well identified at the Ploemeur site from tilt observations (Figure 4a). The pumping rate is not continuously maintained at a static running level, but it is modulated to replenish municipal supply reservoirs instead. One of the three pumps is used to adjust pumping rates on a daily basis. Piezometric levels are fluctuating accordingly with an amplitude of about 2–3 m in the fault zone and tilt measurements at the two stations are well correlated to these pressure variations (Figure 4a). In general, the amplitude of tilt at LB1 represents systematically about 30% of the amplitude recorded at LB2 CW. Hence at the Ploemeur site, the hydromechanical monitoring of loading-unloading cycles is consistently repeatable. Nonetheless, caution in analyzing tilt data must be taken because two issues might alter this repeatability. First, tiltmeters are recording earth tides generated by lunisolar attraction. The earth tide waves, which are composed of a multitude of different fundamental harmonics that can be filtered out

from any given time series (Pawlowski et al., 2002). Problems however, arise when earth tides share roughly the same frequency and magnitude than the targeted hydraulic signals. Unfortunately, this is the case at the Ploemeur site because pumping cycles and the two main earth tide waves sometimes occur at approximately the same frequency (about 6 and 12 h period). Although tidal analysis is carried out on a long time period (several weeks) including a time period without daily pumping, some earth tide residuals might remain in the filtered tilt signals, resulting in difficulties to interpret the exact amplitude associated with pumping or recovery. Second, LB2 is more prone to technical failure or malfunctioning than LB1 as the soil is a less stable environment. In fact, bubbles might appear in the tube between two vessels of the instrument (Figure 3). This delays noticeably the tiltmeter's response to deformation as the bubbles add considerable friction to fluid flow in the instrument's tubes when it seeks to achieve equilibrium. This occurred for instance in the time series of LB2 CE between 8 and 10 days in Figure 4a. Consequently, a thorough

**Table 1**  
Properties of the Long Baseline Tiltmeters Installed at the Ploemeur Site

| Instrument label <sup>a</sup> | Orientation (°E) | Base length (m) | $d_F$ (m) <sup>b</sup> | Measurement range ( $\mu\text{rad}$ ) |
|-------------------------------|------------------|-----------------|------------------------|---------------------------------------|
| <i>LB1 station</i>            |                  |                 |                        |                                       |
| NS                            | N328             | 7.75            | -120                   | 568                                   |
| WE                            | N75              | 32.80           | -120                   | 134                                   |
| <i>LB2 station</i>            |                  |                 |                        |                                       |
| CW                            | N286             | 25.45           | 35                     | N/A                                   |
| CE                            | N286             | 25.55           | 60                     | N/A                                   |
| WE                            | N286             | 51.00           | 47.5                   | 86                                    |

<sup>a</sup>N, S, W, E, and C stand for north, south, west, east, and center, respectively. It refers to the relative position and rough orientation of an instrument's extremities (vessels).

<sup>b</sup>This parameter is an estimate of the shortest horizontal distance between the fault zone's top and the center of the instrument. See Figure 2.

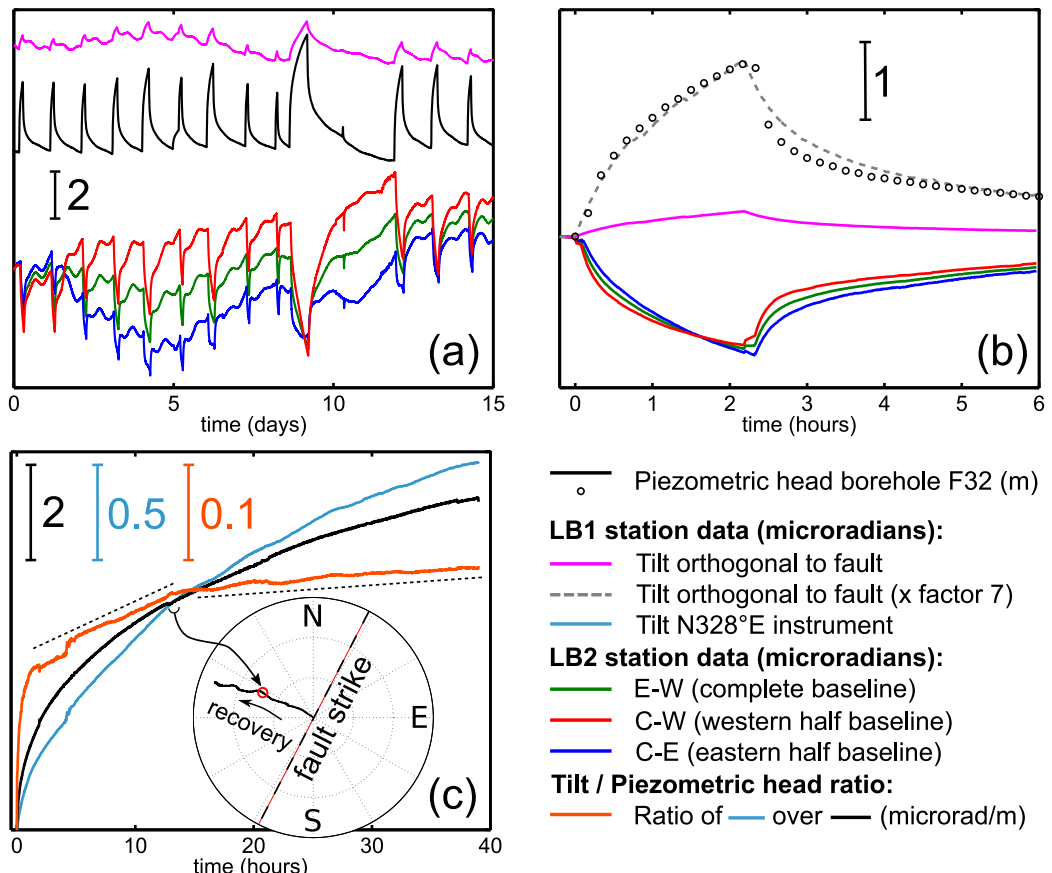


**Figure 4.** Samples of piezometric and clinometric field data acquired at the Ploemeur site (a) over 2 weeks and (b, c) over several hours. The orange curve in Figure 4c is obtained by calculating the ratio of N328°E tilt over piezometric head in F32, or in other words, it is the ratio of the light blue curve over the black curve shown in the same graph. See Figures 1 and 2 for position of borehole F32 and the tiltmeter stations as well as tilt sign convention. The inset in graph Figure 4c is a polar diagram showing the direction of tilt from both instruments at station LB1 during the same time frame (modified after Schuite et al., 2015).

attention has been accorded to these issues by focusing on events where their effect is as small as possible (Figures 4b and 4c).

A typical pumping cycle at the site is shown in Figure 4b. When pumps are turned off, the piezometric level in the fault rises or declines and the tiltmeters are immediately reacting to the subsurface load. This implies that the mechanical stress is nearly instantaneously transmitted through the system at least at the field scale. Furthermore, this kind of hydromechanical monitoring delivers valuable information that may be highlighted with four statements (Figure 4b). (1) The direction toward which LB1 tilts is the opposite of LB2. (2) The amplitude of tilt is different at the two stations. (3) LB2 CW first decreases more rapidly than LB2 CE and at  $t \approx 1.6$  h, the two signals cross each other and LB2 CE becomes smaller than LB2 CW. (4) The transient behavior of tilt closely follows the hydraulic head of the fault zone. One might ask if there are specific conditions or system properties under which the aforementioned observations prevail, or if, on the contrary, they are independent from the aquifer's functioning and rely primarily on its geometrical aspects for example.

Another peculiar feature of field scale hydromechanical observations lies in the ratio of tilt over pressure (Figure 4c), which intuitively reflects the rate of surface deformation per unit fluid pressure change. These different phases can be highlighted in the tilt to pressure ratio. Initially, a rapid nonlinear increase occurs followed by two longer successive linear phases. The latter two are distinguishable by a sudden decrease in slope at  $t \approx 12.5$  h. This denotes a change in hydromechanical behavior of the fractured aquifer as the rate of deformation by unit pressure variation evolves through time. It is important to note that the data

presented in Figure 4c is the result of 39 h of pumping interruption, which has been exceptionally allowed by the authorities for experimental purposes as described in Schuite et al. (2015). At the time of this experiment, station LB1 was only recently installed and LB2 did not yet exist. Besides, we present only the LB1 N328°E data to compute the tilt over pressure ratio. Indeed, his twin is affected by tidal residuals, which blur the interpretation of the ratio. Additionally, we show the evolution of tilt direction from both instruments at station LB1 during the same experiment (inset, Figure 4c). In general, the station tilts perpendicularly to the fault's strike direction as the stress increases. Nevertheless, in a more detailed observation, we may argue that LB1 station deviates noticeably from its original fault-perpendicular trajectory at the same moment the tilt over pressure ratio changes in slope.

In order to understand the transient signature of such coupled surface deformation and aquifer pressure data, we need to seek these behaviors in an equivalent poromechanical model comprising the subvertical fault and surrounding rock, considered here as a homogeneous porous medium (Figure 2).

### 3. Theoretical Framework

#### 3.1. Governing Equations of the Hydromechanical Problem

The hydromechanical problem needs four coupled equations: one describing the flow field and three describing the displacement field across the porous rock body.

First, water flow through saturated porous media is expressed by Darcy's law:

$$\vec{q} = -\frac{K_h}{\gamma_w} \vec{\nabla} p, \quad (1)$$

where  $K_h$  is the hydraulic conductivity in m/s,  $\gamma_w$  the specific weight of water in N/m<sup>3</sup>,  $p$  the pore pressure, and  $\vec{q}$  is known as Darcy's velocity, which can be seen as the fluid's apparent velocity through a porous body in m/s. In any given volume of the system, fluid mass balance must be ensured: the difference between the quantity of fluid leaving and entering the control volume must equal the quantity that is stored in it or released by it. This condition can be stated by the following fluid continuity equation valid for any control volume in the system,

$$\frac{\partial \xi}{\partial t} + \vec{\nabla} \cdot \vec{q} = Q, \quad (2)$$

where the first term  $\partial \xi / \partial t$  stands for the increment of fluid content per unit time and  $Q$  is a source or sink term. As defined by Wang (2000) after Rice and Cleary (1976),  $\xi$  can be regarded as a change of fluid mass content  $\delta m_w$  inside a bulk volume of porous material normalized by its density at a reference state  $\rho_{w0}$ , as  $\xi = \delta m_w / \rho_{w0}$ . Combining equations (1) and (2), yields

$$\frac{\partial \xi}{\partial t} = \frac{K_h}{\gamma_w} \nabla^2 p + Q. \quad (3)$$

Equation (3) describes the pressure diffusion in a porous medium and is the first partial differential equation of the coupled poromechanical problem. The term  $\partial \xi / \partial t$  represents the capacity of the medium to store or release water and thereby, it intrinsically carries a double mechanical meaning. On the one hand, it reflects the ability of the medium to create or destroy space available to the pore fluid and on the other hand, it indicates that the fluid itself is able to compress or uncompress within a reference volume. Porous materials have a particular structure made of some volume occupied by rock minerals  $V_r$  and some volume occupied by the fluid  $V_w$  and are therefore characterized by poroelastic properties. These specific mechanical features can be defined at least theoretically and in some sense during laboratory experiments. Accordingly, it is more convenient to express the increment of fluid content over time as (Wang, 2000)

$$\frac{\partial \xi}{\partial t} = S_\epsilon \frac{\partial p}{\partial t} + \alpha \frac{\partial \epsilon}{\partial t}, \quad (4)$$

where  $\epsilon$  denotes the volumetric strain,  $\alpha$  is referred to as the Biot-Willis coefficient, and  $S_\epsilon$  is the so-called specific storage at constant strain. If  $V$  is the bulk volume of any given porous material, the volumetric strain is simply defined as

$$\epsilon \equiv \frac{\delta V}{V} = \epsilon_{11} + \epsilon_{22} + \epsilon_{33}. \quad (5)$$

The components  $\epsilon_{kk}$  are extensional strains for the  $k$ th axis in the coordinate system. The strain tensor can be written as a function of the spatial derivatives of displacements  $u_k$  in the  $k$ -direction  $x_k$ :

$$\epsilon_{ij} = \frac{1}{2} \left( \frac{\partial u_i}{\partial x_j} + \frac{\partial u_j}{\partial x_i} \right). \quad (6)$$

By looking at equation (4), it is straightforward to understand the physical meaning of both  $S_\epsilon$  and  $\alpha$ . They represent the increment of fluid content in a control volume given by a unit increase of, respectively, pore pressure at constant strain and strain at constant pressure. However, these poroelastic parameters are not easily measured in laboratory experiments for instance, because it is difficult to maintain effectively constant strain and constant pressure conditions. Instead, it is often easier to identify the mechanical behavior of a sample rock volume as a whole or of its parts, namely the fluid phase and the solid mineral phase. Elastic constants which are commonly used are Young's modulus  $E$ , Poisson's ratio  $\nu$  (drained), and the rock grains' bulk compressibility  $1/K_g$ . In addition, the poroelastic behavior of the medium is defined by the compressibility of the fluid  $1/K_w$  and the porosity  $\phi$  which in saturated conditions equals  $V_w/V$ . Assuming a constant porosity over time, which is a reasonable for a mechanically homogeneous rock or a rock made of grains of equal bulk compressibilities (Berryman, 1992), we may derive an expression for both  $S_\epsilon$  and  $\alpha$  as a function of these aforementioned parameters. From Wang (2000; equations (2), p. 33, 3.8, p. 49, and 3.42, p. 57 with the hypothesis  $K_\phi = K_g$ ,  $K_\phi$  being the pore compressibility at constant confining stress and pore pressures), one could show that

$$S_\epsilon = \frac{\alpha}{K_g} + \phi \left( \frac{1}{K_w} - \frac{1}{K_g} \right) \quad (7)$$

and

$$\alpha = 1 - \frac{E}{3(1-2\nu)K_g}. \quad (8)$$

Furthermore, just like fluid continuity is explicitly described in equation (2), there must be a condition on the mechanical state of a given control volume of porous rock. Usually, it is considered that a force equilibrium prevails at any moment in time. In other words, the total stress applied on a rock volume is balanced between the part born by the solid and the part born by the fluid so that all forces sum up to zero (Wang, 2000). Hence, it is assumed that for any mechanical change in a control volume, the equilibrium of all forces is made instantaneously. This is expressed by a set of three equations completing the hydromechanical coupling summarized as (Burbey, 2008; Wang, 2000)

$$\frac{E}{2+2\nu} \left( \nabla^2 u_i + \frac{1}{(1-2\nu)} \frac{\partial^2 u_k}{\partial x_i \partial x_k} \right) = \alpha \frac{\partial p}{\partial x_i}. \quad (9)$$

In summary, the coupled hydromechanical problem exposed here has two variables ( $p$  and  $u$ ) and relies on seven physical parameters ( $K_h$ ,  $\gamma_w$ ,  $K_g$ ,  $E$ ,  $\nu$ ,  $\phi$ , and  $K_w$ ). The term  $Q$  in equation (3) may act as a boundary condition representing the imposed flux due to the injection or withdrawal of fluid at a well for example.

### 3.2. Pressure Diffusion and the Hydrogeological Point of View

It is more common for hydrogeologists to reason in terms of specific storage to represent the poromechanical behavior of an aquifer, instead of the parameters mentioned above. Specific storage  $S_s$  is a measure of how much fluid can be stored into a bulk volume of the medium in response to a unit increase of head. From Wang (2000), one can show that

$$S_s = \gamma_w \left[ \frac{\alpha^2(1+\nu)(1-2\nu)}{E(1-\nu)} + \phi \left( \frac{1}{K_w} - \frac{1}{K_g} \right) \right]. \quad (10)$$

Then the hydraulic diffusivity  $D$  of a medium is defined as

$$D = \frac{K_h}{S_s} \propto \frac{L^2}{t}, \quad (11)$$

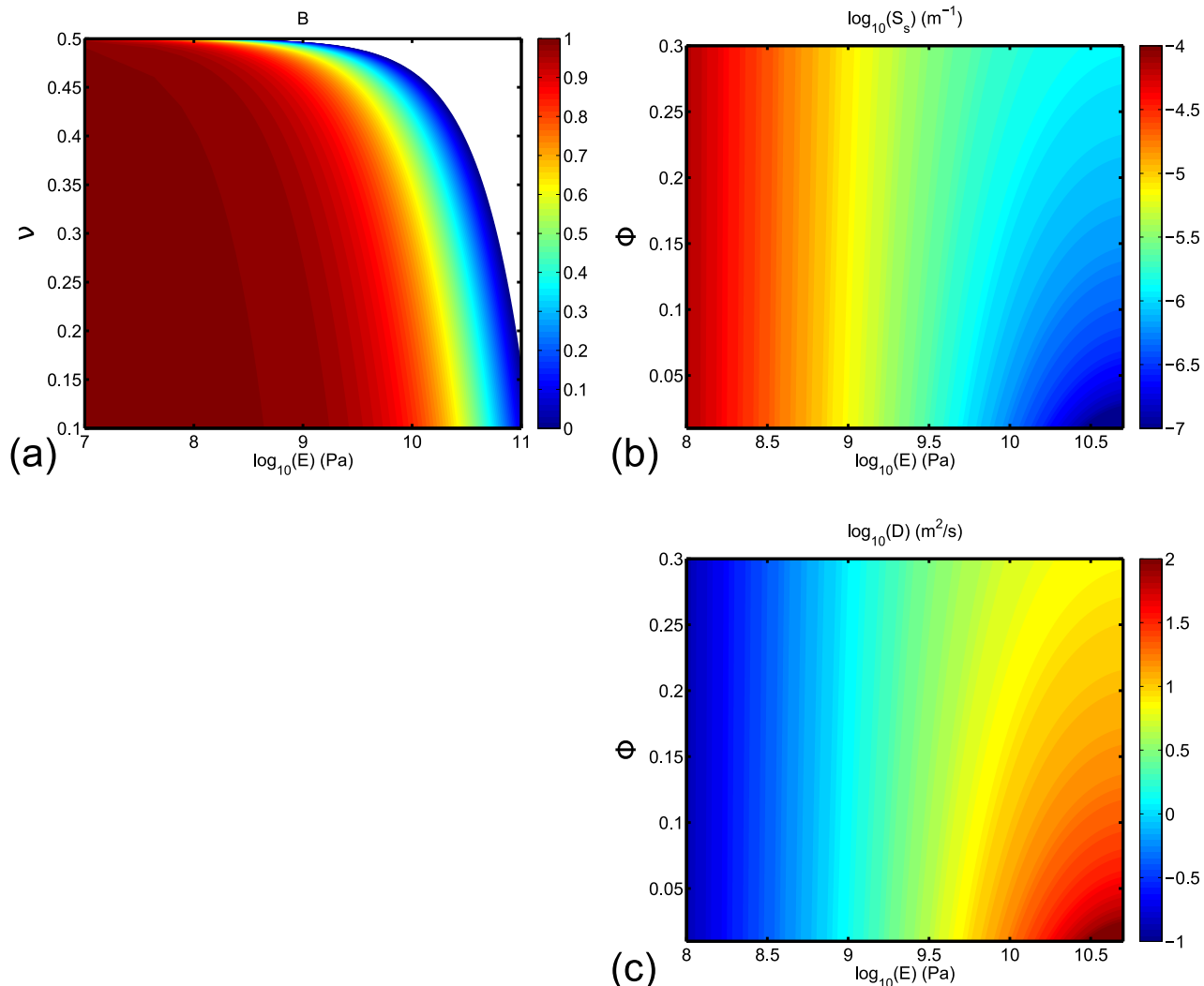


**Figure 5.** Colored contours of (a) Skempton's coefficient  $B$  as a function of Poisson's ratio  $\nu$  and the base 10 logarithm of Young's modulus  $E$ ; (b, c) log of specific storage  $S_s$  and hydraulic diffusivity  $D$  as a function of porosity  $\phi$  and the log of Young's modulus  $E$ .  $K_g = 50 \text{ GPa}$  for all calculations,  $\phi = 0.1$  in (Figure 5a),  $\nu = 0.3$  in (Figures 5b and 5c) and  $K_h = 10^{-5} \text{ m/s}$ .

where  $t$  is time and  $L$  is the distance from the perturbation source to the pressure front in an idealized 2-D flow configuration.

At this point, it is important to note that on a purely theoretical basis, a pressure load in a medium with high specific storage is not necessarily going to yield a larger deformation than a medium having a low specific storage (e.g., in tight rocks). This is because the medium will accommodate the load in terms of an expansion of the bulk rock volume and a compression of the water. As the latter does not generate any observable deformation, it is important to identify from the medium's properties what makes up the storativity: to what extent is the rock expanding and the water compressing for any increase in pressure? Therefore, a physical parameter to describe this partition is needed: Skempton's coefficient  $B$ , which may be expressed in undrained conditions as

$$B = \frac{\frac{1}{K} - \frac{1}{K_g}}{\frac{1}{K} - \frac{1}{K_g} + \phi \left( \frac{1}{K_w} - \frac{1}{K_g} \right)}, \quad (12)$$

with

$$K = \frac{E}{3(1-2\nu)}, \quad (13)$$

defined as the bulk modulus (Detournay & Cheng, 1993; Wang, 2000). Skempton's coefficient  $B$  must be comprised between 0 and 1. When  $B = 1$ , any change in pressure results solely in a deformation of the medium and to the contrary, when  $B = 0$ , only the fluid compresses to accommodate the load. Usually in saturated soils,  $B$  is very close to 1 because  $K$  is 2 or 3 orders of magnitude smaller than  $K_g \sim 10$  GPa whereas  $K_w = 2.2$  GPa. Therefore in this case,  $1/K_g$  may be neglected and the numerator almost equals the denominator in equation (12). However, in stiffer media like crystalline rocks  $K \sim K_g$  and the denominator in 12 becomes significantly larger than the numerator providing there is some significant porosity.

Having  $K_g$  fixed to 50 GPa, Skempton's coefficient  $B$  is mainly sensitive to Young's modulus  $E$  for Poisson's ratio  $\nu \leq 0.4$  (Figure 5a). Similarly, specific storage  $S_s$  is mostly sensitive to Young's modulus  $E$  until  $E \simeq 3$  GPa (Figure 5b). Beyond this value, porosity starts to have a significant impact on specific storage and hydraulic diffusivity  $D$  (Figures 5b and 5c). Ultimately, the amplitude of flow and ground deformation caused by a pressure variation within common reservoirs may be reduced to a function of  $E$  when it is more than an order of magnitude below the grain's bulk modulus  $K_g$ . Then, when  $E$  gets closer to  $K_g$ , deformation is mainly controlled by porosity  $\phi$  and Young's modulus  $E$ , and it is modulated by Skempton's coefficient  $B$ .

## 4. Modeling Strategy

### 4.1. Numerical Modeling

We use the finite element modeling (FEM) software ABAQUS (version 6.13) to numerically solve the partial differential equations (3) and (9) for pore pressure and displacement, in response to an induced flow in a dipping fault, embedded in a homogeneous isotropic hardrock unit. As we are interested in the transient behavior of this system and because we expect the fault to generate an asymmetry in the pressure field, we consider a 3-D model as illustrated in Figure 6. The overall domain is a parallelepiped sized  $3 \times 3 \times 1$  km and is compartmentalized into three subdomains, each bearing the properties of the associated hydrogeological entity. First, the fault zone has an extension of a 1,000 m along its strike direction and 500 m along its dip direction. Its dip is set to  $70^\circ$  and it has a width of 30 m. The top of the fault is separated from the surface by a subdomain of constant thickness (30 m) representing a confining layer, thus acting as an impermeable barrier. The rest of the domain constitutes the host rock in which the fault is nested. Hence, all subdomains are modeled as equivalent porous media with distinct hydromechanical properties.

Mechanical boundary conditions are set as follows (Figure 6): all sides are constrained in the horizontal directions ( $x-y$  plane,  $U_x = U_y = 0$ ) whereas the bottom face is constrained in the vertical direction  $z$  ( $U_z = 0$ ). The upper surface and the rest of the domain are free to move in all directions. As for the hydraulic boundary conditions, the pressure is maintained constant at the sides of the domain ( $p = 0$ ) and there is no flow through the bottom and through the aforementioned upper confining layer ( $dp/dt = 0$ ). The hydraulic perturbation is imposed as a constant seepage velocity  $q_i = -0.008$  m/s at 130 m below the surface at the injection point (Figure 6). All modeling experiments simulate 30 h of injection. Furthermore, the pressure field across the model is monitored relatively to its initial state, which is set to 0 Pa everywhere. Finally, the whole domain is fully saturated from the beginning and throughout the simulations. This is a reasonable assumption given the confined behavior of the system.

We tested different parameter sets as presented in Tables 2 and 3. Some parameters remain the same in all models: the matrix's elastic properties ( $E_m = 35$  GPa and  $\nu_m = 0.27$  based on borehole seismic data conducted at the Ploemeur site, and  $K_g = 50$  GPa), and the top layer is given the same properties than the rock matrix, except for its permeability which is maintained very low ( $K_h = 10^{-22}$  m/s).

A tetrahedral mesh is used to discretize the domain with a refinement forced around the injection point (characteristic length  $\delta_c = 3$  m) and the fault domain ( $5 \text{ m} \leq \delta_c \leq 10 \text{ m}$ ). Mesh size is increased

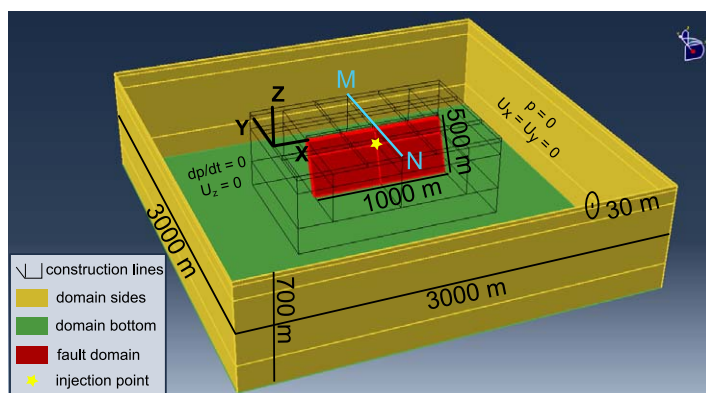


**Figure 6.** Geometry and boundary conditions of the finite element model used in the study.

**Table 2**  
Parameter Values Attributed to the Fault Zone for the Different Models Presented in the Study

| Parameters | $E_f$ | $v_f$ | $\phi_f$ | $K_f$ | $B_f$ | $K_{h,f}$            | $S_{s,f}$             | $D_f$             |
|------------|-------|-------|----------|-------|-------|----------------------|-----------------------|-------------------|
| Units      | GPa   |       |          | GPa   |       | m/s                  | 1/m                   | m <sup>2</sup> /s |
| M1         | 1.0   | 0.4   | 0.20     | 1.67  | 0.870 | $1.0 \times 10^{-5}$ | $5.13 \times 10^{-6}$ | 1.95              |
| M2         | 0.10  | 0.4   | 0.20     | 0.17  | 0.986 | $1.0 \times 10^{-5}$ | $4.63 \times 10^{-5}$ | 0.22              |
| M3         | 5.0   | 0.4   | 0.20     | 8.33  | 0.535 | $1.0 \times 10^{-5}$ | $1.49 \times 10^{-6}$ | 6.73              |
| M4         | 0.10  | 0.4   | 0.20     | 0.17  | 0.986 | $1.0 \times 10^{-4}$ | $4.63 \times 10^{-5}$ | 2.16              |
| M7         | 0.10  | 0.4   | 0.20     | 0.17  | 0.986 | $1.0 \times 10^{-5}$ | $4.63 \times 10^{-5}$ | 0.22              |
| M8         | 0.10  | 0.4   | 0.20     | 0.17  | 0.986 | $1.0 \times 10^{-5}$ | $4.63 \times 10^{-5}$ | 0.22              |
| M10        | 10.0  | 0.4   | 0.20     | 16.67 | 0.315 | $1.0 \times 10^{-5}$ | $1.05 \times 10^{-6}$ | 9.48              |
| M11        | 10.0  | 0.4   | 0.20     | 16.67 | 0.315 | $1.0 \times 10^{-5}$ | $1.05 \times 10^{-6}$ | 9.48              |
| M12        | 10.0  | 0.4   | 0.33     | 16.67 | 0.218 | $1.0 \times 10^{-5}$ | $1.61 \times 10^{-6}$ | 6.22              |
| M13        | 10.0  | 0.4   | 0.33     | 16.67 | 0.218 | $1.0 \times 10^{-5}$ | $1.61 \times 10^{-6}$ | 6.22              |
| M14        | 1.0   | 0.4   | 0.33     | 1.67  | 0.802 | $1.0 \times 10^{-5}$ | $5.68 \times 10^{-6}$ | 1.76              |
| M15        | 10.0  | 0.4   | 0.80     | 16.67 | 0.103 | $1.0 \times 10^{-5}$ | $3.61 \times 10^{-6}$ | 2.77              |
| M16        | 10.0  | 0.4   | 0.80     | 16.67 | 0.103 | $1.0 \times 10^{-5}$ | $3.61 \times 10^{-6}$ | 2.77              |
| M18        | 7.0   | 0.4   | 0.33     | 11.67 | 0.314 | $1.0 \times 10^{-5}$ | $1.79 \times 10^{-6}$ | 5.59              |
| M22        | 0.10  | 0.4   | 0.10     | 0.17  | 0.993 | $1.0 \times 10^{-3}$ | $4.59 \times 10^{-5}$ | 21.81             |
| M26        | 7.0   | 0.4   | 0.33     | 11.67 | 0.314 | $1.0 \times 10^{-5}$ | $1.79 \times 10^{-6}$ | 5.59              |
| M28        | 0.05  | 0.2   | 0.20     | 0.03  | 0.998 | $5.0 \times 10^{-4}$ | $1.77 \times 10^{-4}$ | 2.82              |
| M34        | 0.60  | 0.4   | 0.20     | 1.0   | 0.919 | $1.0 \times 10^{-4}$ | $8.17 \times 10^{-6}$ | 12.24             |
| M35        | 0.80  | 0.4   | 0.20     | 1.33  | 0.894 | $1.0 \times 10^{-4}$ | $6.27 \times 10^{-6}$ | 15.96             |

Note.  $B_f$ ,  $S_{s,f}$ , and  $D_f$  are calculated from equations (12), (10), and (11), respectively.

toward the domain's sides and bottom ( $100 \text{ m} \leq \delta_c \leq 150 \text{ m}$ ). This results in a total of 1.6 million tetrahedral elements over the whole domain, which is a large number for the problem in consideration here. Usually, the meshing size emerges from the right compromise between good numerical convergence and accuracy, and reasonable computing costs. In our model, the main issues were to deal with the geometry of the heterogeneity (dipping fault) and with the transition between regions with very different mesh sizes. In particular, we wanted to have a typical element length at the free surface close to the fault that was similar

to the spacing between two vessels of a tiltmeter on the field, so that measured and modeled tilt series could be consistently comparable. Another specificity in our procedure is the need of a relatively small time step to capture the targeted processes compared to common problems in hydrogeology. Combined with fact that the 3-D domain had to remain large enough so that boundary conditions have limited influence on the simulation's results, all the necessary constraints could not be met without a large mesh. Fortunately, models were run on a shared memory supercomputing system at Virginia Tech (USA). Using 24 processors in parallel, it took about 10 h to complete each run, which was reasonable for us. However, it is worth pointing out that depending on the objectives and by applying an extensive mesh study, a lighter model could be designed for cases where supercomputing resources are not available.

#### 4.2. Normalization and Comparison With Field Data

In order to compare field data time series and model outputs, we define a characteristic diffusion time  $t_D$  that corresponds to the time the pressure front needs to reach the fault zone's lateral edges. From equation (11), we have

$$t_D = \frac{L_f^2}{4D_f}, \quad (14)$$

where the subscript  $f$  refers to the fault's properties and  $L_f$  is the total fault length along strike direction. Whereas  $L_f$  is fixed and known in

**Table 3**  
Parameter Values Attributed to the Rock Matrix for the Different Models Presented in the Study

| Parameters | $\phi_m$ | $B_m$ | $K_{h,m}$             | $S_{s,m}$             | $D_m$             |
|------------|----------|-------|-----------------------|-----------------------|-------------------|
| Units      |          |       | m/s                   | 1/m                   | m <sup>2</sup> /s |
| M1         | 0.05     | 0.472 | $1.0 \times 10^{-7}$  | $2.67 \times 10^{-7}$ | 0.3741            |
| M3         | 0.05     | 0.472 | $1.0 \times 10^{-7}$  | $2.67 \times 10^{-7}$ | 0.3741            |
| M4         | 0.05     | 0.472 | $1.0 \times 10^{-7}$  | $2.67 \times 10^{-7}$ | 0.3741            |
| M7         | 0.05     | 0.472 | $1.0 \times 10^{-8}$  | $2.67 \times 10^{-7}$ | 0.0374            |
| M8         | 0.01     | 0.899 | $1.0 \times 10^{-7}$  | $7.57 \times 10^{-8}$ | 1.3210            |
| M10        | 0.05     | 0.472 | $1.0 \times 10^{-8}$  | $2.67 \times 10^{-7}$ | 0.0374            |
| M11        | 0.01     | 0.899 | $1.0 \times 10^{-7}$  | $7.57 \times 10^{-8}$ | 1.3210            |
| M12        | 0.1      | 0.309 | $1.0 \times 10^{-7}$  | $4.8 \times 10^{-7}$  | 0.2082            |
| M13        | 0.1      | 0.309 | $1.0 \times 10^{-8}$  | $4.8 \times 10^{-7}$  | 0.0208            |
| M14        | 0.1      | 0.309 | $1.0 \times 10^{-7}$  | $4.8 \times 10^{-7}$  | 0.2082            |
| M15        | 0.05     | 0.472 | $1.0 \times 10^{-7}$  | $2.67 \times 10^{-7}$ | 0.3741            |
| M16        | 0.01     | 0.817 | $1.0 \times 10^{-7}$  | $9.7 \times 10^{-8}$  | 1.0310            |
| M18        | 0.2      | 0.183 | $1.0 \times 10^{-8}$  | $9.06 \times 10^{-7}$ | 0.0110            |
| M22        | 0.01     | 0.817 | $1.0 \times 10^{-7}$  | $9.7 \times 10^{-8}$  | 1.0310            |
| M26        | 0.01     | 0.817 | $1.0 \times 10^{-10}$ | $9.7 \times 10^{-8}$  | 0.0010            |
| M28        | 0.01     | 0.817 | $1.0 \times 10^{-7}$  | $9.7 \times 10^{-8}$  | 1.0310            |
| M34        | 0.01     | 0.817 | $1.0 \times 10^{-7}$  | $9.7 \times 10^{-8}$  | 1.0310            |
| M35        | 0.01     | 0.817 | $1.0 \times 10^{-7}$  | $9.7 \times 10^{-8}$  | 1.0310            |

Note.  $B_m$ ,  $S_{s,m}$ , and  $D_m$  are calculated from equations (12), (10), and (11), respectively.

the model (1,000 m), it is not known for the field. However,  $D_{f,M}$  can be calculated from equations (10) and (11) (second subscript  $M$  stands for "model"). For the field, we have retained a value of  $D_{f,F}=22 \text{ m}^2/\text{s}$  from pumping test data (second subscript  $F$  stands for "field"). Then, we systematically adjust  $L_{f,F}$  so that the time series match.

Model pressure outputs  $p_M^*(t)$  are normalized as follows:

$$p_M^*(t) = \frac{p_M(t) \times \max(p_{F32})}{p_M(t_e)}, \quad (15)$$

where  $p_{F32}$  stands for the pressure recorded on the field in borehole F32 (Figure 1) and  $t_e$  is the last simulation time.

The comparison of modeled tilt versus observed tilt is more subtle because the instruments integrate the response of the whole 3-D structure and it is a gradient of the surface vertical displacement. One way of looking at this problem is to consider a tiltmeter's *angle of vision*. We suppose that to be comparable, two different tiltmeters monitoring two different faults have to incorporate the response of the deforming region from the same point of view (see supporting information). In other words, the extent of the pressure front in the fault must be seen at a tilt station from the same perspective in all cases. Therefore, we compare the modeled tilt at a horizontal distance  $d_M$  from the fault's top (see Figure 2) to the observed tilt with

$$d_M = d_F \times \frac{L_{f,M}}{L_{f,F}}. \quad (16)$$

Note that in this study, all tilt observations (in models and on the field) lie in the near-field region as defined by Lecampion et al. (2005) because  $d/L_f < 1.5$ . In such conditions, tilt measurements were shown to be sensitive to the lateral extent of the pressurized source (Lecampion et al., 2005; Lecampion & Peirce, 2007).

To simplify the analysis, we compare field data projected on a direction perpendicular to the fault zone, to model outputs obtained on the M-N survey line shown in Figures 2 and 6. In doing so, we may collapse tilt data from the two instrument of LB1 and perform all the analysis on a reference survey line, which is assumed to be closely matching field conditions (Figures 1 and 2).

## 5. Results

### 5.1. Pressure and Surface Deformation Fields

In Figures 7 and 8, we show typical pressure and surface deformation maps from two models with very different properties (M10 and M22) and at two different times: first after 1.6 h of injection and then at the very end of the simulation, i.e., after 30 h. As presented in Tables 2 and 3, M10 has a fault zone a 100 times more rigid than M22. Also, the hydraulic conductivity of the fault is 2 orders of magnitude higher for M22, whereas the ratio  $D_f/D_m$  is 2 orders of magnitude higher for M10.

These contrasts in properties can be perceived from pressure and deformation maps, even at early times after injection starts (Figure 7). Results show that the pressure front has already reached the fault's edges at  $t = 1.6 \text{ h}$  for M22, which is not the case for M10 due to its lower fault diffusivity  $D_f$ . In fact the contrast in hydraulic conductivity  $K_f$  is distinguishable as well, from the larger pressure gradients that may be noticed near the injection point in M10 both at early and late times, unlike what is observed in M22 where pressure gradients are smoother along the fault (Figures 7 and 8, map 1). This is of course a direct consequence of Darcy's law (equation (1)) given that the flux remains the same. Seemingly, the pressure perturbation progresses more easily in the matrix in M22 which has a lower hydraulic diffusivity contrast between fault and matrix, and therefore displays a lower aspect ratio of the pressure field than does M10. In any case though, these pressure fields remain symmetric with respect to the fault's strike direction.

Surface deformation responses between M10 and M22 are very different as well. At early times (Figure 7, map 2), M10 displays an eye-shaped vertical displacement pattern that lies on top of the fault zone, slightly off toward the dipping flank. As for M22, the main vertically displacement pattern forms a large lobe on the dipping side of the fault, and a second lobe on the other side with much lower amplitude. The asymmetry in  $Y$  direction is to be attributed to the significant fault dip (Longuevergne et al., 2009). The extension of displacement fields is correlated to the pressure front's extent in the fault, as the eye-shaped pattern of

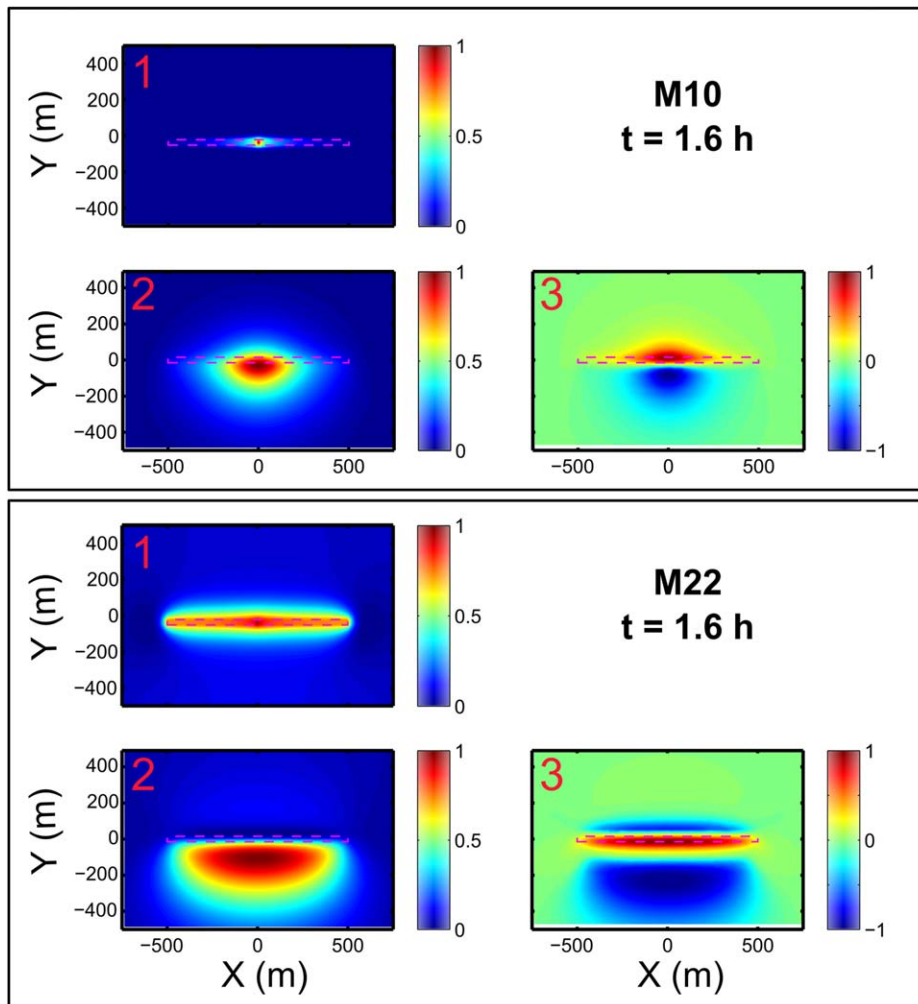


**Figure 7.** (1) Typical pressure, (2) surface vertical displacement, and (3) surface tilt maps for two models, M10 and M22 after 1.6 h of injection. The magenta dashed lines display the position of the fault zone.  $X$  and  $Y$  represent the direction along the fault's strike, and perpendicular to the strike, respectively. The pressure maps are taken from the horizontal plane at a depth corresponding to the injection point. Tilt maps are taken as the gradient of vertical displacement along the  $Y$  direction and are scaled between  $-1$  and  $1$ , making sure that the sign of initial unscaled tilts are respected. All other fields are scaled between  $0$  and  $1$ .

M10 stretches along the strike direction with time for instance. At the end of the simulation, vertical displacement patterns are more similar in both models unlike in the early time of injection. The only main differences are the position of their maxima with respect to the fault and their aspect ratio. Hence, it seems hardly feasible to constrain the hydromechanical properties of a fault zone from vertical displacement maps alone.

Tilt measurements however, have by definition the advantage of having a strong sensitivity to gradients of vertical displacement and therefore they can take on positive or negative values. In M10 (Figures 7 and 8, map 3), tilt fields form two slightly asymmetric lobes of opposite sign where in M22, three lobes of alternating sign prevail, with high positive values of top of the fault's roof. This demonstrates that the shape of tilt patterns is more discriminatory than surface displacement patterns in regards to fault zone properties. Besides, maximum vertical displacements in both models are just below a millimeter at the end of the simulation where maximum tilts are on the order of  $1\text{--}10 \mu\text{rad}$  (not shown here). Submillimeter precision is not achievable by common geodetic methods, especially at these times scales, whereas microradians are easily detected by most surface tiltmeters nowadays. This observation once again underscores the benefit of using surface tiltmeters to monitor hydraulic experiments in fault zones. We now want to address the

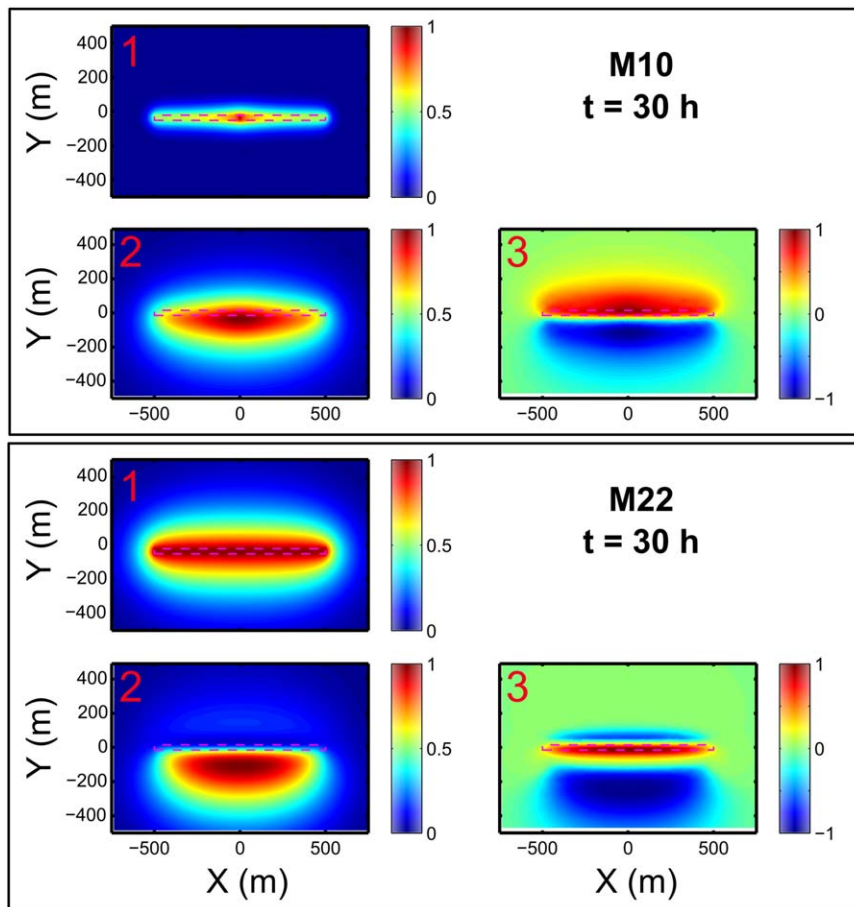


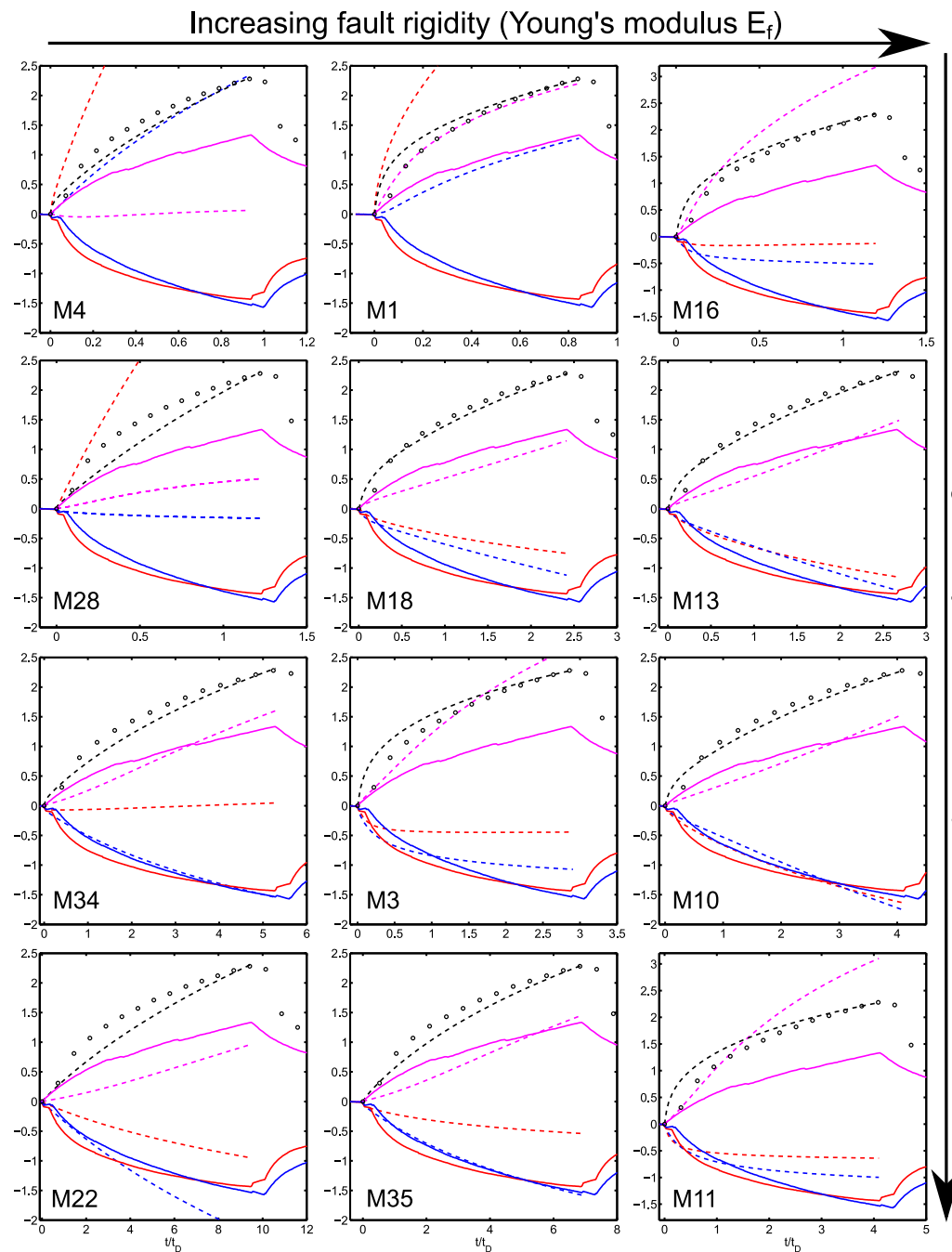
**Figure 8.** (1) Typical pressure, (2) surface vertical displacement, and (3) surface tilt maps for two models, M10 and M22 after 30 h of injection. The magenta dashed lines display the position of the fault zone.  $X$  and  $Y$  represent the direction along the fault's strike, and perpendicular to the strike, respectively. The pressure maps are taken from the horizontal plane at a depth corresponding to the injection point. Tilt maps are taken as the gradient of vertical displacement along the  $Y$  direction and are scaled between  $-1$  and  $1$ , making sure that the sign of initial unscaled tilts are respected. All other fields are scaled between  $0$  and  $1$ .

question of the information content in transient tilt measurements and assess its potential to unravel the system's hydromechanical functioning.

### 5.2. Information Content of Transient Tilt

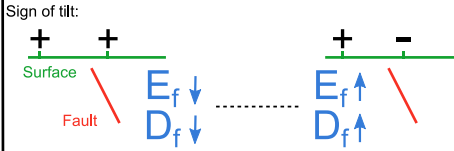
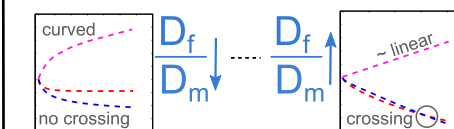
One of our objectives is to seek what information surface tilt data may bear about hydromechanical properties of a fault zone reservoir. A comparison of field data and various representative modeled outputs is displayed in Figure 9 as a function of relative fault rigidity and diffusivity. For all models shown, F32 head variations are relatively well described by the model. Though, the surface deformation on both sides of the fault shows very different responses. From this perspective and as could be sensed from deformation maps (Figures 7 and 8), tilt observations may be able to rule out hydromechanical configurations. Indeed, all models with low fault diffusivity ( $D_{f,M} \leq 2 \text{ m}^2/\text{s}$ ) and low fault rigidity ( $E_f \leq 1 \text{ GPa}$ ) produce surface tilts with an opposite sign compared to those observed on the field at LB2 (M1 and M4). Moreover, M4 generates almost no tilt at all at LB1. Note that in these simulations, the pressure front does not even reach the fault's edges ( $t/t_D < 1$ ).

For low values of  $E_f$  but high values of  $D_f$  (M34, M35, and M22), the sign of the tilts are the same as field measurements but the difference between LB2 station's two halves is growing rapidly with time. The opposite seems to predominate when  $E_f$  is large but  $D_f$  is low (M16), where LB1 tilt is largely overestimated by the model and the difference in the two modeled LB2 responses is rapidly attaining a plateau. In



**Figure 9.** Comparison of surface tilt and piezometric head time series between field data and various representative numerical model outputs, as a function of fault rigidity (or Young's modulus  $E$ ) and fault diffusivity  $D_f$ . The latter classification is valid only by rows or by columns, and not necessarily transversally.  $x$  axis:  $t/t_D$ ;  $y$  axis: Tilt in  $\mu\text{rad}$  or pressure in m. Color codes are basically the same as in Figure 4: plain lines are for tilt observations from the field, dashed lines are model outputs. Magenta: LB1 tilt orthogonal to fault which has been multiplied by 4 for better visibility; blue: C-E LB2 tilt; and red: C-W LB2 tilt. Black circles are piezometric head data from borehole F32 and the black dashed line is its equivalent in the model as defined in equation (15).

intermediate cases like M3, both the plateau and relatively large difference in LB2 tilts' responses can be observed. Moreover, one may notice that the dynamic responses of M16 and M11 are almost identical except for the maximum modeled LB2 responses which differ by a factor 2. In fact,  $D_f$  in M16 is 3.5 times lower than in M11 which itself has a fault diffusivity twice the one of M22. Again, this demonstrates that the

| Evidence   | Primary control    | Tendency   |
|--|--------------------|--|
| Sign<br>(= direction of tilt)  | Hydro - mechanical | <p>Sign of tilt:<br/> </p> |
| Evolution of difference between the two "half" LB2 tiltmeter time series with time | Mechanical         |                            |
| Crossing of LB2 time series and shape of LB1 time series                           | Hydro - dynamical  |                            |

**Figure 10.** Potential factors shaping the surface tilt responses. Light blue arrows specify if the properties are tending toward high or low values respectively. The sign convention for tilt is illustrated in Figure 2.

temporal evolution of tilt at the surface near a fault, especially the difference in response between two successive tiltmeters above the slab (LB2) and the amplitude of a tiltmeter on the other side (LB1), encompasses information about the mechanical properties of the fault independently of its diffusivity; and independently of the diffusivity of the matrix too (Tables 2 and 3).

Another important feature of the data has been reproduced by three models: the crossing of the two LB2 time series (M10 and M13, as well as M11 at very early times, Figure 9). M10 and M13 diverge mainly by their fault diffusivity which is due to a 65% relative difference in fault porosity (Table 2). The amplitude of modeled LB1 tilt is the same for both, but the curve crossing of LB2 time series arrives later in M10 and their amplitude is slightly higher and closer to the observed tilts. Besides, M10 and M13 have low matrix diffusivity compared to numerous other models displayed in Figure 9 ( $D_{m,M} \sim 10^{-2}$ ), except M18. Hence, the ratio  $D_f/D_m$  seems to control the occurrence of tilt series' crossing at LB2, at least partly. Nevertheless, even if the pressure response, tilt amplitudes and occurrence of LB2 time series' crossing is best reproduced by M10, the modeled tilt responses are almost linear and therefore they do not exhibit properly the dynamic responses observed on the field, which are of square root shape. In this regard, the temporal shape of the tilt is better represented by M11 and M16 for LB1, and by M35 for LB2 CE for instance.

A summary of the different factors shaping the tilt response, based on the previous comparative analysis between modeling results is shown in Figure 10 (including models not presented in Figure 9). Accordingly, the natural fault zone at Ploemeur should be rather stiff and have a large diffusivity whereas the one of the surrounding media should be comparatively low (Figures 2, 4, and 10).

### 5.3. Information Content of Tilt/Pressure Ratio

If one has precise and high frequency measurements of both surface deformation and groundwater pressure, it is interesting to investigate the tight link between both quantities through time as a pressure perturbation progresses in the fractured reservoir. We argue that one way of doing it, is to combine these quantities into one variable. Consequently, we define  $\tau^*$  as the ratio of modeled tilt over modeled hydraulic head at positions equivalent to those of LB1 and F32 in the Ploemeur field, respectively. In addition,  $\tau^*$  is scaled between 0 and 1 to facilitate comparison between different models. Two examples are given in Figure 11 and all models presented in this study show an equivalent behavior (data not shown here). This ratio has an evolution through time that is similar to the one observed in the field (Figure 4c). These figures show that our models are able to reproduce the two asymptotic behaviors distinguished in the ratio, except for very early times. However, unlike what is perceived on the field, the transition phase between the two linear behaviors is longer (Figure 11).

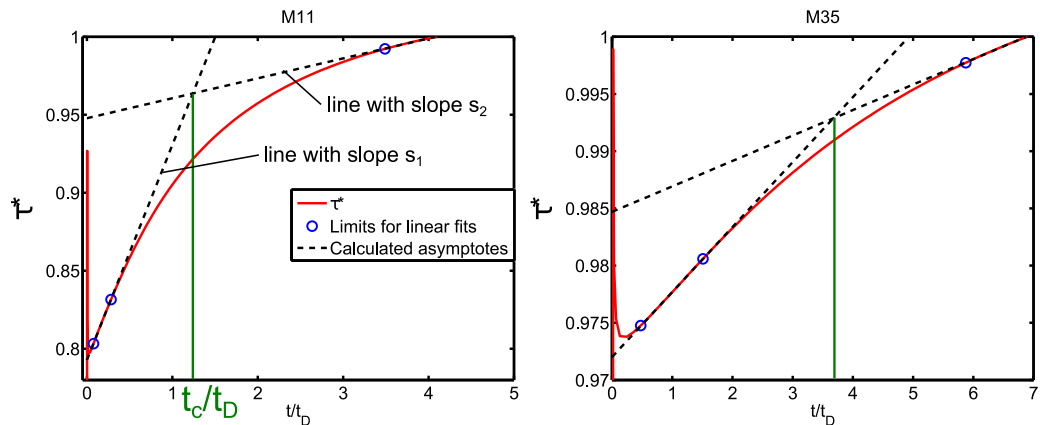


**Figure 11.** Ratio of tilt over hydraulic head  $\tau^*$  as a function of normalized time for two different models. The normalized critical time  $t_c/t_D$  is here defined as the time when the asymptotes (dashed lines) cross.

Usually, asymptotic behaviors characterize the functioning of complex systems that undergo competing processes. The transition from one asymptotic behavior to another may be interpreted as a mutation from one state of the system, where some processes may prevail, to a different state of functioning, where other processes dominate over the previous ones. Here we seek to separate the processes that shape the temporal and asymptotic behavior of the hydromechanical response comprised in tilt/pressure ( $T/P$ ) ratios. In order to do so, we represent the hydromechanical functioning of system by two elastic models and each one is intended to mimic one process. First, the elastic effect of pressure diffusion in the fault zone is represented by the lateral growth of a mode I dislocation plane (Okada, 1985). Second, the mechanical response of the matrix is accounted for by the volumetric eigenstrain source of Mogi (1958) as illustrated in Figure 12. In other words, both these models consider a semi-infinite elastic half-space in which the source of deformation is either the opening of a plane with prescribed geometry (Okada source, see Schuite et al., 2015), or a spherical source (Mogi). Representing the hydromechanical problem with such models might be a crude approximation of natural processes, but the advantage here is given by their simplicity that allows for the explicit illustration of two end-member hydromechanical behaviors. We chose the numerical model M22 as a reference model because it is has both high fault diffusivity and high Skempton's coefficient, which is necessary to justify the use of Okada's elastic model (Figure 14). Taking the transient pressure response in the fault from M22 as input, we let the Okada plane grow laterally as a function of  $\sqrt{D_f t}$  (classical for flow in porous media, see de Marsily, 1986). The mode I opening of the dislocation plane  $\delta_o$  (Okada, 1985) is calculated as

$$\delta_o(t) = p_M(t) \times \frac{30}{E_f}. \quad (17)$$

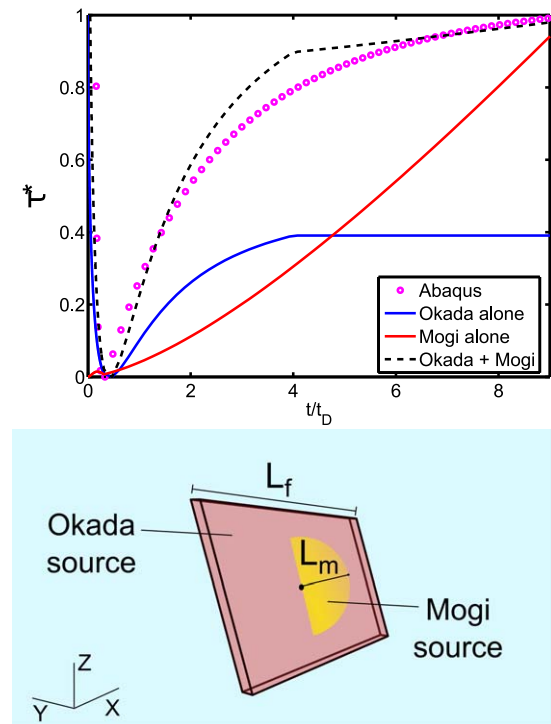


**Figure 12.** Separation of processes shaping the temporal behavior of the tilt/pressure ratio  $\tau^*$ . (top half)  $\tau^*$  as a function of dimensionless time for different models. The data denoted "Abaqus" refers to numerical model M22. "Okada" and "Mogi" are two elastic models that mimic the pressure diffusion and associated deformation of the fault and the matrix, respectively (as sketched under the graph). The Okada plane is growing along strike direction following  $L_f(t) = \sqrt{D_f t}$ . Seemingly, we impose  $L_m(t) = \sqrt{D_m t}$ .

The factor 30 corresponds to the width of the fault zone in meters; hence, the ratio  $30/E_f$  is comparable to the inverse of fault normal stiffness, commonly used in fault mechanics (e.g., Guglielmi et al., 2015). The center of the Mogi source corresponds to the centroid of the Okada plane. Furthermore, the radius of the sphere increases as a function of  $\sqrt{D_m t}$ . The pressure input is also  $p_M(t)$  but modulated through time by a complementary error function (erfc) scaled between 0 and 1, to account for the fact the pressure applied uniformly in Mogi's source must somehow decrease as the sphere of

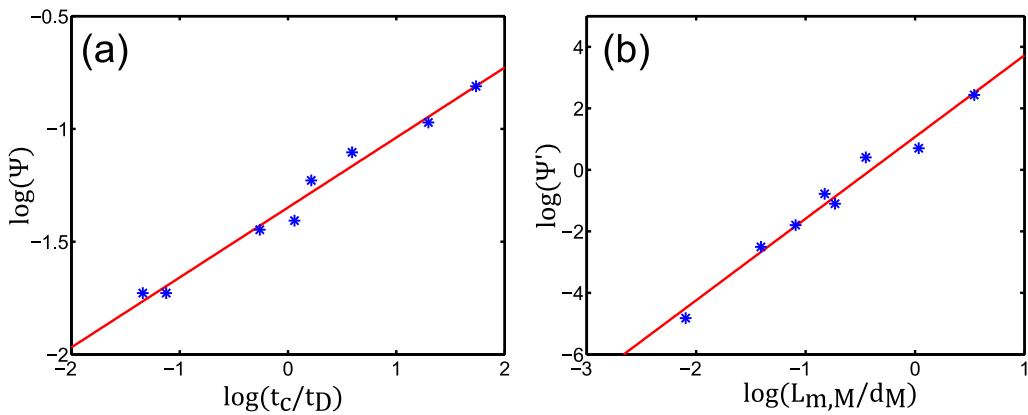


**Figure 13.** Identification of the link between  $t_c$ ,  $s_1$ , and  $s_2$  of the ratio  $\tau^*$  (see Figure 11) and some dynamic properties of the reservoir. Each blue star is the result of one numerical model and the red line is the fitted power law as defined by (a) equation (18) and (b) equation (19). Models M3, 11, 13, 15, 16, 22, 34, and M35 were used here.

influence grows. Note that the erfc function appears in the Theis solution of the equation of pressure diffusion in isotropic homogeneous porous media, in radial form (de Marsily, 1986). As a result, a combination of these two analytical models describes very well the behavior of the ratio  $\tau^*$  of M22 (Figure 12). Indeed, it captures correctly the transition from one dominant hydromechanical behavior to another: (1) in the first stage of the experiment, pressure propagates rapidly in the conductive fault zone which controls strong temporal deformation gradients; (2) then the pressure front reaches the fault's lateral edges, which would result in no further increase of the  $T/P$  ratio in the simple elastic representation of the fault (Figure 12, blue curve), because then, deformation rates are only generated by an increment in mode I opening, but no longer by an increment in lateral extent of the fluid pressure-induced in-plane deformation front; and (3) at some point, pressure diffusion in the matrix is sufficiently developed to contribute solely to surface deformation, which maintains the  $T/P$  ratio increasing with time but at a lower rate until the end of the experiment (Figure 12, red curve).

Hence, the evolution in shape of  $T/P$  ratios through time displays sensitivity to the hydrodynamic functioning of the fault zone system where a competition between 2-D-fracture and 3-D-reservoir diffusion prevails. In order to investigate more deeply the information content of  $\tau^*$ , we define three indices that can

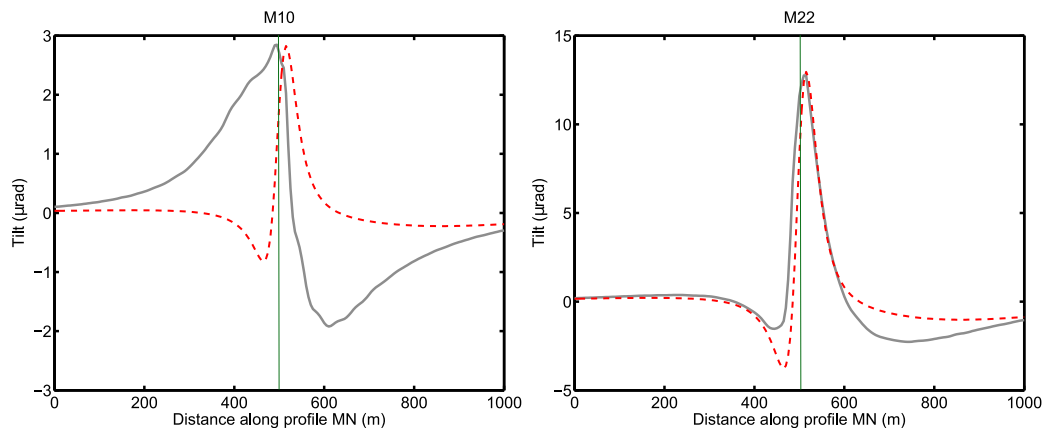


**Figure 14.** Tilt profiles along survey line M-N illustrated in Figures 2 and 6 for two representative models (situation at the simulation's final iteration): M10 has a rigid fault zone ( $E_f = 10$  GPa), contrarily to M22 ( $E_f = 0.1$  GPa). The grey line is the profile obtained from the numerical model and the dashed red line is the equivalent calculated from the analytical solution of Okada (1985). This analytical solution (left) fails to capture the profile of the rigid fault case but (right) matches reasonably well the case where Skempton's coefficient is high in the fault, except for the amplitude of the negative depressions on each side of the narrow central peak.

systematically be measured: the slopes  $s_1$  and  $s_2$  of the two asymptotes followed by the ratio, and  $t_c$  the time at which the two asymptotes intersect one another as illustrated in Figure 11. When analyzed under certain conditions, these indices collapse around two empirical power laws as shown in Figure 13 and expressed as

$$\Psi = \frac{d_M}{L_{f,M}} = c_1 \left( \frac{t_c}{t_D} \right)^{c_2} \quad (18)$$

and

$$\Psi' = \frac{s_2 D_{f,M}}{s_1 D_{m,M}} = c'_1 \left( \frac{L_{m,M}}{d_M} \right)^{c'_2}, \quad (19)$$

where

$$L_{m,M} = \sqrt{D_{m,M} \times t_D} \quad (20)$$

corresponding to the characteristic diffusion length in the matrix during a characteristic diffusion time  $t_D$  defined in (14).  $c_1$ ,  $c_2$ ,  $c'_1$ , and  $c'_2$  are coefficients calculated by linear regression for which we obtained  $c_1=0.26$ ,  $c_2=0.31$ ,  $c'_1=2.92$ , and  $c'_2=2.66$ . Also, we saw that  $t_c/t_D$  grows linearly with the horizontal distance between fault roof and tilt observation point, in each individual model (not shown here).

Hence, these relationships reveal the systematic link that exists between some properties of the faulted reservoir and the indices observed in the ratio tilt over pressure  $\tau^*$ . In particular, the asymptotic behaviors evidenced in the ratio  $\tau^*$ , seem to be mainly controlled by the hydrodynamical properties of the medium, namely the ratio of fault and matrix diffusivities. Moreover, it demonstrates that the information embodied in the system's transient hydromechanical behavior reflects primarily how, when and where the pressure diffuses in a dual fracture-matrix system. It does not necessarily rely on the fact that the fault's lateral edge have been reached by the pressure front, because models for which  $t_c/t_D < 1$  fit well using (18) and (19). It is also not directly dependent on particular poromechanical properties, because any combination of them may explain the dynamics of the system as they disappear behind the specific storage  $S_s$ , and thus behind diffusivity  $D$ .

## 6. Discussion

### 6.1. Benefits of Transient Hydromechanical Experiments and Modeling

Instead of seeking the perfect match between numerical modeling results and field data, this study focuses on the information content that might be found in the temporal shape of hydromechanical observations. Indeed, the complexity of the natural system under consideration, involving numerous mechanical interactions and heterogeneous flow structure, makes it challenging to fully explain surface deformation measurements at the Ploemeur site. However, we show from modeling experiments that the general functioning and hydromechanical properties of such a reservoir have a special signature in the transient evolution of surface tilt time series. In many studies, geodetic data are used to strengthen parameter estimation in inversion schemes because they constitute an independent additional constraint on the medium's mechanical response to hydraulic loading. There is no denying that data inversions are insightful techniques that provide knowledge on a reservoir's state properties (see Binley et al., 2015 and references therein). Nevertheless, inversion analysis offers only little information about a system's behavior in time, unlike what we have demonstrated in the present study.

#### 6.1.1. Tiltmetry as a Tool for Reservoir Mechanics

The sign of tilt series as well as their shape already reveal the mechanical framework in which the studied faulted system lies in: from the "almost" purely elastic to the nearly poroelastic extreme cases. In fact, some patterns are characteristic of a rigid fault zone and thus a low Skempton coefficient  $B_f$  whereas others are typical of a nonrigid fault with  $B_f \simeq 1$  (see Figure 10). In the case of a fault or fracture seen as a planar permeable discontinuity embedded in a much less permeable rock, a Skempton coefficient equal to 1 signifies that any pressure variation in the fault results solely in the deformation of its walls and thus, the surrounding medium. Hence, fluid pressure is translated as a stress normal to the fracture plane. This is why in this case, the Okada (1985) solution approximates correctly the numerical model outputs (Figure 14) as it is the

elastic situation. On the other hand, a poroelastic behavior comes into play when the rigidity of the fault approaches the rigidity of the rock medium. Then, the poroelastic term in the expression of Skempton's coefficient (equation (12)) is not negligible any longer and any pressure change generates a significant compression of water.

We have shown that these extreme cases may be well captured by surface tilt measurements from the field setting at the Ploemeur site from both sides of the fault zone. This observation has an important implication as regards the modeling objectives and procedure. As numerical modeling can become quite complicated (geometry, discretisation, computing cost, number of parameters, etc.), it might be interesting to know whether a fault has a pure elastic behavior, because if it is so, analytical solution of elastic deformation might be sufficiently well suited to interpret surface deformation data. Conversely, if this is not the case, the use of Okada's solution might lead to severe misinterpretation of such data.

Based on comparisons between the investigated models and surface deformation measurements, we show that the subvertical fault of Ploemeur's aquifer is stiff and has a high diffusivity contrast between fault and matrix. Le Borgne et al. (2006) have found from hydraulic testing that indeed, there is a significant heterogeneity in hydrodynamic properties across the field and from one scale of investigation to another. In particular, these authors found that the storativity  $S = S_{se}$  (with  $e$  the characteristic thickness of the medium) varies from  $10^{-5}$  to  $10^{-3}$  from cross-borehole flowmeter tests conducted along the fault zone. For long-term pumping tests, the interval for storativity  $S$  is reduced and the mean value is increased ( $10^{-4}$  to  $4 \times 10^{-3}$ ). Such a high variability in the estimations, typical of fractured aquifers, might be explained in part by the sensitivity of specific storage  $S_s$  to porosity when the fault is stiff (Figure 5b). For instance, if we retain a median value of  $S \simeq 10^{-4}$  in a 30 m thick fault zone, and considering that it is indeed stiff as suggested by the hydromechanical evidence presented here, so that  $E_f = 10$  GPa, the porosity of the fault would need to be approximately 80% which is an unrealistically high value. Conversely, retaining a value of 20% porosity in these conditions would yield  $S \simeq 3 \times 10^{-5}$ . Hence from a theoretical perspective, it appears that achieving good estimates of a fault's porosity in a such context is hardly feasible. On one hand, the system may be purely elastic and strain is insensitive to porosity ( $B = 1$ ). On the other hand, the heterogeneity yields field estimates of  $S$  from hydraulic tests that are broadly distributed, so that complementary and independent estimates from hydromechanical tests are not sufficient to narrow down the incertitude on porosity.

#### 6.1.2. Tiltmetry to Understand Reservoir Hydraulics

Being able to follow subsurface processes in time is a key asset in reservoir engineering. For example, in geothermal reservoirs, one of the processes of interest is the geomechanical response of the formation to changes in temperature that might reactivate faults. In this context, Im et al. (2017) have recently calculated that surface tiltmeters may be suited to record deformation associated with such processes. Moreover, many authors have demonstrated that relative geodetic instruments provide useful information on the hydrogeological properties of shallower reservoirs during field hydraulic experiments (e.g., Barbour & Wyatt, 2014; Burbey et al., 2012; Schuite et al., 2015, 2017; Schweisinger et al., 2011; Svenson et al., 2008; Vasco et al., 2001). Yet the detailed behavior of surface deformation with respect to subsurface fluid flow in fractured media is not completely understood. In particular, Schuite et al. (2015) underscored the difficulty in explaining surface tilt data during long hydraulic tests. To the best of our knowledge, we have unraveled for the first time the information content on fractured reservoir hydrodynamics that can be found in combined transient tilt and pressure data. We would argue that this type of analysis adds considerable value to the use of tiltmeters in a context of reservoir monitoring. These instruments are sensitive to contrasts in subsurface properties (here fault zone versus matrix) as much as they are sensitive to subsurface processes (here the evolution in hydromechanical regime). Indeed, we show from numerical simulations that the ratio tilt/pressure encompasses information on the diffusivity contrast between the fault and matrix and that the evolution of this ratio through time follows two end-member asymptotic behaviors: the first is mainly controlled by pressure diffusion in the fault whereas the second is governed by pressure diffusion in the matrix. This seems to be valid regardless of the mechanical settings. Also, tilt data may contribute to estimate the lateral extent of a fault zone and more interestingly, our results suggest that it may be achieved even when the pressure front does not reach the fault's edges. Consequently, it may be possible to accurately monitor the propagation of fluids in complex reservoirs without the need of numerous costly boreholes. In the context of deep CO<sub>2</sub> storage for example, operators want to make sure that the fluid does not leak through faults from the target geological unit to upper undisturbed units. From our results, we would argue that the

use of surface tiltmeters may help diagnosing such a hazard since transient tilt time series hold information on flow transition between compartments with distinct hydraulic properties.

## 6.2. Disregarded Effects and Limits

### 6.2.1. Discontinuities

In the model we implemented, the top 30 m thick top layer is given the mechanical properties of the porous rock medium but has been assigned a negligible permeability. This is because the LB1 station is directly attached to granitic rock and because it limits numerical instabilities at the interface between this unit and the rest of the domain. Hence, this layer acts as a barrier for flow but does not block the mechanical propagation of the perturbation. Nonetheless, the effect of its mechanical properties has been discarded in this study, even if the LB2 tilt station is installed in the ground and thus, in some material that is significantly softer than granite or mica-schist. This might alter tilt profiles across the fault zone and therefore it should affect to some extent how LB1 and LB2 tilts may be interpreted by such a model.

Seemingly, we did not account for the mechanical discontinuity between granite and mica-schist. The matrix domain is treated as a single entity. The mechanical properties of these two types of rock are in the same order of magnitude (Wang, 2000) but the transition between them might have a different behavior. It would be arduous to treat such discontinuity in the model since it does not appear homogeneous across the field and has a complex geometry (Ruelle et al., 2010). Nevertheless, Ruelle et al. (2010) showed that this contact zone is subhorizontal and LBHTs are poorly sensitive to extended horizontal features.

### 6.2.2. Geometry

We have focused our study on a single geometry of the system, namely with fixed fault dip, lateral and root extents. Tilt is mainly sensitive to the dip angle and root length (Longuevergne et al., 2009). Consequently any variation on these parameters would change the amplitudes of surface tilts and the degree of asymmetry in M-N tilt profiles (Figure 14) and thereby the patterns at observations points equivalent to LB1 and LB2 are expected to change accordingly as well. However, the main processes and general hydromechanical behavior are expected to remain the same. In particular, surface deformation patterns are likely to remain as presented in Figure 8 as long as the studied fault is not close to horizontality. Then, similar shapes of transient tilts as the ones presented in Figure 9 should be found almost unchanged but at different distances from the fault zone. Moreover, the fitting coefficients in the power laws 18 and 19 linking  $T/P$  ratio's shape to reservoir properties are probably dependent on the geometry too, but we expect them to remain power laws. Nonetheless, this is something for further investigation. Despite the geometry dependency of our results, we can make the safe assertion that surface tilt measurement would still prove to add valuable constraints on any similar system's hydrodynamic functioning and hydromechanical properties.

### 6.2.3. Domain Approach

In the numerical study of the hydromechanical experiment, the fault is treated as a domain or, in other words, as a volume that has distinct properties from the surrounding rock domain. For simplicity and commodity, we did not include anisotropy in key properties either in the fault or in the matrix. To some extent, it seems reasonable to treat the large matrix volume with average, isotropic and homogeneous properties, but a fault zone intrinsically represents heterogeneity within the broader domain. Even if it might increase complexity, this effect should probably be investigated but is far beyond the scope of our study.

Moreover, the shape of the fault zone domain, especially the edges, might have mechanical effects that are difficult to evaluate. However, the elastic solution of Okada (1985) closely approximates the tilt profile of low rigidity faults (Figure 14). Hence, we are confident that observations made near the center of the fault zone and thus far enough from lateral borders are sufficiently reliable.

## 7. Summary and Conclusion

In this study, we have presented surface tilt data recorded at the Ploemeur fractured aquifer observatory (France). These measurements allow for the precise monitoring of deformation provoked by man-made hydraulic perturbations at hourly time scales. Indeed, the transient tilt patterns are very well correlated to piezometric level fluctuations in the fault zone. The responses of the two tiltmeters LB1 and LB2, one on each side of the fault and at different distances from its roof, are different in amplitude and take opposite signs. Besides, the ratio of LB1 tilt over pressure in the fault zone during a typical hydraulic test, shows a very peculiar trend through time. It comprises two consecutive linear phases suggesting the presence of

two hydromechanical regimes in the system's behavior. From these observations, we built an interpretation scheme based on 3-D poroelastic numerical models that includes two main domains with distinct properties: the fault zone and the surrounding rock medium. We simulated 30 h of transient injection at a point in the fault, and we analyzed pressure and deformation outputs from various combinations of hydromechanical properties, in order to assess the information content of transient tilt measurements in such context.

By comparing all models and by confronting them to field data, we showed that transient surface tilt measurements near a fault zone are sensitive to geometrical, mechanical and hydrodynamical properties of the system. We demonstrated that having tiltmeters placed on each side of the fault is crucial to obtain reasonable constraints on these characteristics. In particular, we showed that tilt/pressure ratios encompass information on the dynamic behavior of the system, as well as specific properties of the system such as the hydraulic diffusivity contrast between fault and matrix. These characteristics are not directly dependent on the elastic properties of the medium. Besides, we argue that achieving a good estimate of porosity seems hardly feasible from tilt and hydraulic data in faulted aquifer settings, unless the fault is very rigid ( $E_f > 10$  GPa) and if independent estimates of storativity come with low uncertainty (which is to our knowledge rarely the case in fractured media).

In a nutshell, simple hydromechanical tests in fault zone involving surface tilt measurements offer a significant insight into its overall dynamic functioning and properties. Surprisingly, tiltmeters are noninvasive tools that seem even more suited to fractured hydrogeology than fault hydromechanics at the  $\sim 10^2$  to  $10^3$  m scale, because they display stronger sensitivity to hydrodynamical properties than poroelastic properties.

## Notation

### Meaning of Main Subscripts

- $f$  refers to a property of the fault zone.
- $m$  refers to a property of the rock matrix.
- $F$  refers to a field property.
- $M$  refers to a model property.

### List of Mathematical Symbols, With Significance and Units

#### Latin Letters

|             |   |
|-------------|---|
| $B$         | Skempton's coefficient, dimensionless.  |
| $c_1, c'_1$ | fitting coefficients, dimensionless.  |
| $c_2, c'_2$ | fitting exponents, dimensionless.   |
| $D$         | hydraulic diffusivity, $\text{m}^2/\text{s}$ .                                      |
| $d_F$       | horizontal distance between tiltmeter and the fault's roof in the field, m.         |
| $d_M$       | horizontal distance between tiltmeter and the fault's roof in the model, m.         |
| $E$         | Young's modulus, Pa.  |
| $K$         | bulk modulus of porous material, Pa.  |
| $K_g$       | bulk modulus of rock grains (Pa), noted $K'_s$ in Wang (2000).                      |
| $K_h$       | hydraulic conductivity, $\text{m}/\text{s}$ .                                       |
| $K_w$       | bulk modulus of water, Pa.  |
| $L$         | distance from perturbation source to pressure front, m.                             |
| $L_b$       | baseline length of a long-base tiltmeter, m.  |
| $L_f$       | length of fault zone along strike direction, m.                                     |
| $L_m$       | distance from perturbation source to pressure front in the matrix at $t = t_D$ , m. |
| $p$         | water pressure, Pa or m.  |
| $p_{F32}$   | hydraulic head or pressure measured in borehole F32, Pa or m.                       |
| $p_M$       | pressure from model output, Pa or m.  |
| $p_M^*$     | normalized pressure from model output, Pa or m.                                     |
| $Q$         | source term/volumetric flow rate, $\text{m}^3/\text{s}$ .                           |
| $q$         | Darcy's velocity, $\text{m}/\text{s}$ .   |
| $s_1$       | slope of first $\tau^*$ asymptote.  |
| $s_2$       | slope of second $\tau^*$ asymptote.   |
| $S$         | storativity, dimensionless.   |

|              |   |
|--------------|---|
| $S_\epsilon$ | specific storage at constant strain, $\text{m}^{-1}$ .              |
| $S_s$        | specific storage in the hydrogeological sense, $\text{m}^{-1}$ .    |
| $t$          | time from the beginning of injection, s.                            |
| $t_c$        | critical time of $\tau^*$ asymptotes' crossing, s.                  |
| $t_D$        | characteristic time of pressure diffusion along the fault zone, s.  |
| $t_e$        | time at the end of injection, s.                                    |
| $u_k$        | displacement in the $k$ -direction, m.                              |
| $V$          | bulk volume of porous material, $\text{m}^3$ .                      |
| $V_r$        | volume occupied by rock minerals in porous material, $\text{m}^3$ . |
| $(x, y, z)$  | global coordinate system.   |

#### Greek Letters

|                               |   |
|-------------------------------|---|
| $\alpha$                      | Biot-Willis coefficient, dimensionless.                           |
| $\delta_c$                    | characteristic mesh size, m.                                      |
| $\delta_o$                    | magnitude of mode I opening in dislocation plane, m.              |
| $\epsilon$                    | volumetric strain, dimensionless.                                 |
| $\phi$                        | porosity, dimensionless.  |
| $\gamma_w$                    | specific weight of water, $\text{N}/\text{m}^3$ .                 |
| $\nu$                         | Poisson's ratio, dimensionless.                                   |
| $\theta$                      | tilt, rad.  |
| $\tau^*$                      | ratio of tilt over pressure, scaled between 0 and 1.              |
| $\partial \zeta / \partial t$ | increment of water content per unit time, $\text{m}^3/\text{s}$ . |

#### Acknowledgments

This work is part of the ANR project EQUIPEX CRITEX (grant ANR-11-EQPX-0011), the ANR project "Hydrogeodesy" and the ORE H+ observatory network from which it has been supported. J. Schuite's PhD thesis is partly funded by the Brittany Region. Tilt data are available upon request at <http://hplus.ore.fr/>. Virginia Tech's Advanced Research Computing team is warmly acknowledged for granting access to the scientific computing facilities as well as for their technical support. We warmly thank the Associate Editor, Larry Murdoch, and the three anonymous reviewers for providing insightful comments and suggestions that largely improved the quality of the paper. Finally, F. Beauducel is thanked for making available his Matlab packages implementing Okada and Mogi's analytical solutions.

#### References

- Agnew, D. C. (1986). Strainmeters and tiltmeters. *Reviews of Geophysics*, 24(3), 579–624.
- Bandis, S. C., Lumsden, A. C., & Barton, N. R. (1983). Fundamentals of rock joint deformation. *International Journal of Rock Mechanics and Mining Science & Geomechanics Abstracts*, 20(6), 249–268.
- Barbour, A. J., & Wyatt, F. K. (2014). Modeling strain and pore pressure associated with fluid extraction: The Pathfinder Ranch experiment. *Journal of Geophysical Research: Solid Earth*, 119, 5254–5273. <https://doi.org/10.1002/2014JB011169>
- Barton, N. R., Bandis, S. C., & Bakhtar, K. (1985). Strength, deformation and conductivity coupling of joints. *International Journal of Rock Mechanics and Mining Science & Geomechanics Abstracts*, 22(3), 121–140.
- Bense, V. F., Gleeson, T., Loveless, S. E., Bour, O., & Scibek, J. (2013). Fault zone hydrogeology. *Earth Science Reviews*, 127, 171–192.
- Berkowitz, B. (2002). Characterizing flow and transport in fractured geological media: A review. *Advances in Water Resources*, 25, 861–884.
- Berryman, J. G. (1992). Effective stress for transport properties of inhomogeneous porous rock. *Journal of Geophysical Research*, 97(B12), 17409–17424.
- Biessy, G., Moreau, F., Dauteuil, O., & Bour, O. (2011). Surface deformation of an intraplate area from GPS time series. *Journal of Geodynamics*, 52, 24–33.
- Binley, A., Hubbard, S. S., Huisman, J. A., Revil, A., Robinson, D. A., Singha, K., & Slater, L. D. (2015). The emergence of hydrogeophysics for improved understanding of subsurface processes over multiple scales. *Water Resources Research*, 51, 3837–3866. <https://doi.org/10.1002/2015WR017016>
- Bonnet, E., Bour, O., Odling, N. E., Davy, P., Main, I., Cowie, P., & Berkowitz, B. (2001). Scaling of fracture systems in geological media. *Reviews of Geophysics*, 39(3), 347–383.
- Boudin, F., Bernard, P., Longuevergne, L., Florsch, N., Larmat, C., Courteille, C., . . . Kammentaler, M. (2008). A silica long base tiltmeter with high stability and resolution. *Review of Scientific Instruments*, 79(3), 034502.
- Boussinesq, J. (1868). Mémoire sur l'influence des frottements dans les mouvements réguliers des fluides. *Journal de mathématiques pures et appliquées*, 2, 13, 377–424.
- Burbey, T. J. (2008). The influence of geologic structures on deformation due to ground water withdrawal. *Ground Water*, 46(2), 202–211.
- Burbey, T. J., Hisz, D., Murdoch, L. C., & Zhang, M. (2012). Quantifying fractured crystalline-rock properties using well tests, earth tides and barometric effects. *Journal of Hydrology*, 414–415, 317–328.
- Cappa, F., Guglielmi, Y., Graffet, S., Lançon, H., & Lamarque, I. (2006a). Use of in situ fiber optic sensors to characterize highly heterogeneous elastic displacement fields in fractured rocks. *International Journal of Rock Mechanics and Mining Sciences*, 43(4), 647–654.
- Cappa, F., Guglielmi, Y., Rutqvist, J., Tsang, C.-F., & Thoraval, A. (2006b). Hydromechanical modeling of pulse tests that measure both fluid pressure and fracture-normal displacement of the Coaraze Laboratory site, France. *International Journal of Rock Mechanics and Mining Sciences*, 43, 1062–1082.
- Chaussard, E., Bürgmann, R., Shirzaei, M., Fielding, E. J., & Baker, B. (2014). Predictability of hydraulic head changes and characterization of aquifer-system and fault properties from InSAR-derived ground deformation. *Journal of Geophysical Research: Solid Earth*, 119, 6572–6590. <https://doi.org/10.1002/2014JB012166>
- Chen, H. C., Kümpel, H.-J., & Krawczyk, C. M. (2010). Field layout of a tiltmeter array to monitor micro-deformation induced by pumping through a horizontal collector well. *Near Surface Geophysics*, 8, 321–330.
- Cornet, F. H. (2016). Seismic and aseismic motions generated by fluid injections. *Geomechanics for Energy and the Environment*, 5, 42–54.
- Davies, R., Foulger, G., Bindley, A., & Styles, P. (2013). Induced seismicity and hydraulic fracturing for the recovery of hydrocarbons. *Marine and Petroleum Geology*, 45, 171–185.
- De Marsily, G. (1986). *Quantitative hydrogeology: Groundwater hydrology for engineers*. New York, NY: Academic Press.

- Detournay, E., & Cheng, A. H.-D. (1993). Fundamentals of poroelasticity. In J. A. Hudson (Ed.), *Comprehensive rock engineering: Principles, practice and projects* (Vol. 2, pp. 113–171). Oxford, UK: Pergamon Press.
- Elkoury, J. E., Brodsky, E. E., & Agnew, D. C. (2006). Seismic waves increase permeability. *Nature*, 441(29), 1135–1138.
- Elkoury, J. E., Niemeijer, A., Brodsky, E. E., & Marone, C. (2011). Laboratory observations of permeability enhancement by fluid pressure oscillation in situ fractured rock. *Journal of Geophysical Research*, 116, B02311. <https://doi.org/10.1029/2010JB007759>
- Fabian, M., & Kümpel, H.-J. (2003). Poroelasticity: Observations of anomalous near surface tilt induced by ground water pumping. *Journal of Hydrology*, 281, 187–205.
- Galloway, D. L., & Hoffmann, J. (2007). The application of satellite differential SAR interferometry-derived ground displacements in hydrogeology. *Hydrogeology Journal*, 15(1), 133–154.
- Guglielmi, Y., Elsworth, D., Cappa, F., Henry, P., Gout, C., Dick, P., & Durand, J. (2015). In situ observations on the coupling between hydraulic diffusivity and displacements during fault reactivation in shales. *Journal of Geophysical Research: Solid Earth*, 120, 7729–7748. <https://doi.org/10.1002/2015JB012158>
- Hisz, D. B., Murdoch, J. C., & Germanovich, L. N. (2013). A portable borehole extensometer and tiltmeter for characterizing aquifers. *Water Resources Research*, 49, 7900–7910. <https://doi.org/10.1002/wrcr.20500>
- Im, K., Elsworth, D., Guglielmi, Y., & Mattioli, G. S. (2017). Geodetic imaging of thermal deformation in geothermal reservoirs—Production, depletion and fault reactivation. *Journal of Volcanology and Geothermal Research*, 338, 79–91.
- Jiménez-Martínez, J., Longuevergne, L., Le Borgne, T., Davy, P., Russian, A., & Bour, O. (2013). Temporal and spatial scaling of hydraulic response to recharge in fractured aquifers: Insights from a frequency domain analysis. *Water Resources Research*, 49, 3007–3023. <https://doi.org/10.1002/wrcr.20260>
- Karasaki, K., Freifeld, B., Cohen, A., Grossenbacher, K., Cook, P., & Vasco, D. (2000). A multidisciplinary fractured rock characterization study at Raymonde Field Site, Raymond, CA. *Journal of Hydrology*, 236, 17–34.
- Kitagawa, Y., Fujimori, K., & Koizumi, N. (2002). Temporal change in permeability of the rock estimated from repeated water injection experiments near the Nojima fault in Awaji Island, Japan. *Geophysical Research Letters*, 29(10). <https://doi.org/10.1029/2001GL014030>
- Le Borgne, T., Bour, O., de Dreuzy, J.-R., Davy, P., & Touchard, F. (2004). Equivalent mean flow models for fractured aquifers: Insights from a pumping tests scaling interpretation. *Water Resources Research*, 40, W03512. <https://doi.org/10.1029/2003WR002436>
- Le Borgne, T., Bour, O., Paillet, F. L., & Caudal, J.-P. (2006). Assessment of preferential flow path connectivity and hydraulic properties at single-borehole and cross-borehole scales in a fractured aquifer. *Journal of Hydrology*, 328, 347–359.
- Lecampion, B., Jeffrey, R., & Detournay, E. (2005). Resolving the geometry of hydraulic fractures from tilt measurements. *Pure and Applied Geophysics*, 162(12), 2433–2452.
- Lecampion, B., & Pearce, A. (2007). Multipole moment decomposition for imaging hydraulic fractures from remote elastostatic data. *Inverse Problems*, 23(4), 1641–1658.
- Leray, S., de Dreuzy, J.-R., Bour, O., & Bresciani, E. (2013). Numerical modeling of the productivity of vertical to shallowly dipping fractured zones in crystalline rocks. *Journal of Hydrology*, 481, 64–75.
- Leray, S., de Dreuzy, J.-R., Bour, O., Labasque, T., & Aquilina, L. (2012). Contribution of age data to the characterization of complex aquifers. *Journal of Hydrology*, 464–465, 54–68.
- Longuevergne, L., Florsch, N., Boudin, F., Oudin, L., & Camerlynck, C. (2009). Tilt and strain deformation induced by hydrologically active natural fractures: Application to the tiltmeters installed in Sainte-Croix-aux-Mines observatory (France). *Geophysical Journal International*, 178, 667–677.
- Mogi, K. (1958). Relations between the eruptions of various volcanoes and the deformations of the ground surfaces around them. *Bulletin of the Earthquake Research Institute of Tokyo*, 36, 99–134.
- Moreau, F., & Dauteuil, O. (2013). Geodetic tools for hydrogeological surveys: 3D-displacements above a fractured aquifer from GPS time series. *Engineering Geology*, 152, 1–9.
- Murdoch, L. C., Freeman, C. E., Germanovich, L. N., Thrash, C., & DeWolf, S. (2015). Using in situ vertical displacements to characterize changes in moisture load. *Water Resources Research*, 51, 5998–6016. <https://doi.org/10.1002/2015WR017335>
- Murdoch, L. C., & Germanovich, L. N. (2006). Analysis of a deformable fracture in permeable material. *International Journal for Numerical and Analytical Methods in Geomechanics*, 30, 529–561.
- Murdoch, L. C., & Germanovich, L. N. (2012). Storage change in a flat-lying fracture during well tests. *Water Resources Research*, 48, W12528. <https://doi.org/10.1029/2011WR011571>
- Neuman, S. P. (2005). Trends, prospects and challenges in quantifying flow and transport through fractured rocks. *Hydrogeology Journal*, 13, 124–147.
- Okada, Y. (1985). Surface deformation due to shear and tensile faults in a half-space. *Bulletin of the Seismological Society of America*, 75(4), 1135–1154.
- Pawlowski, F., Beardsley, B., & Lentz, S. (2002). Classical tidal harmonic analysis including error estimates in MATLAB using T\_TIDE. *Computers & Geosciences*, 28, 929–937.
- Rice, J. R., & Cleary, M. P. (1976). Some basic stress diffusion solutions for fluid saturated elastic porous media with compressible constituents. *Reviews of Geophysics and Space Physics*, 14, 227–241.
- Rojstaczer, S., Wolf, S., & Michel, R. (1995). Permeability enhancement in the shallow crust as a cause of earthquake-induced hydrological changes. *Nature*, 373, 237–239.
- Rothert, E., & Shapiro, S. A. (2003). Microseismic monitoring of borehole fluid injections: Data modeling and inversion for hydraulic properties of rocks. *Geophysics*, 68(2), 685–689.
- Ruelle, S., Moreau, F., Bour, O., Gapais, D., & Martelet, G. (2010). Impact of gently dipping discontinuities on basement aquifer recharge: An example from Ploemeur (Brittany, France). *Journal of Applied Geophysics*, 70, 161–168.
- Rutqvist, J., Noorishad, J., Tsang, C.-F., & Stephansson, O. (1998). Determination of fracture storativity in hard rocks using high-pressure injection testing. *Water Resources Research*, 34(10), 2551–2560.
- Rutqvist, J., & Stephansson, O. (2003). The role of hydromechanical coupling in fractured rock engineering. *Hydrogeology Journal*, 11, 7–40.
- Schuite, J., Longuevergne, L., Bour, O., Boudin, F., Durand, S., & Lavenant, N. (2015). Inferring field-scale properties of a fractured aquifer from ground surface deformation during a well test. *Geophysical Research Letters*, 42, 10696–10703.
- Schuite, J., Longuevergne, L., Bour, O., Guihéneuf, N., Becker, M. W., Cole, M., . . . Boudin, F. (2017). Combining periodic hydraulic tests and surface tilt measurements to explore in situ fracture hydromechanics. *Journal of Geophysical Research: Solid Earth*, 122, 6046–6066. <https://doi.org/10.1002/2017JB014045>
- Schweisinger, T., Svenson, E. J., & Murdoch, L. C. (2009). Introduction to hydromechanical well tests in fractured rock aquifers. *Ground Water*, 47(1), 69–79.

- Schweisinger, T., Svenson, E. J., & Murdoch, L. C. (2011). Hydromechanical behavior during constant-rate pumping tests in fractured gneiss. *Hydrogeology Journal*, 19, 963–980.
- Svenson, E., Schweisinger, T., & Murdoch, L. C. (2008). Field evaluation of the hydromechanical behavior of flat-lying fracture during slug tests. *Journal of Hydrology*, 359, 30–45.
- Vasco, D. W., Karasaki, K., & Kishida, K. (2001). A coupled inversion of pressure and surface displacement. *Water Resources Research*, 37(12), 3071–3089.
- Vasco, D. W., Rucci, A., Ferretti, A., Novali, F., Bissell, R. C., Ringrose, P. S., ... Wright, I. W. (2010). Satellite-based measurements of surface deformation reveal fluid flow associated with the geological storage of carbon dioxide. *Geophysical Research Letters*, 37, L03303. <https://doi.org/10.1029/2009GL041544>
- Vinci, C., Steeb, H., & Renner, J. (2015). The imprint of hydro-mechanics of fractures in periodic pumpings tests. *Geophysical Journal International*, 202, 1613–1626.
- Wang, H. F. (2000). *Theory of linear poroelasticity with applications to geomechanics and hydrogeology*. Princeton, NJ: Princeton University Press.
- Wang, L., & Cardenas, M. B. (2016). Development of an empirical model relating permeability and specific stiffness for rough fractures from numerical deformation experiments. *Journal of Geophysical Research: Solid Earth*, 121, 4977–4989. <https://doi.org/10.1002/2016JB013004>
- Warpinski, N. R., Wolhart, S. L., & Wright, C. A. (2001). *Analysis and prediction of microseismicity induced by hydraulic fracturing*. Paper presented at SPE Annual Technical Conference and Exhibition. Society of Petroleum Engineers.
- Williams-Stroud, S., Ozgen, C., & Billingsley, R. L. (2013). Microseismicity-constrained discrete fracture network models for stimulated reservoir simulation. *Geophysics*, 78(1), B37–B47.
- Witherspoon, P. A., Wang, J. S. Y., Iwai, K., & Gale, J. E. (1980). Validity of cubic law for fluid flow in a deformable rock fracture. *Water Resources Research*, 16(6), 1016–1024.